



## Processes that generate and deplete liquid water and snow in thin midlevel mixed-phase clouds

Adam J. Smith,<sup>1</sup> Vincent E. Larson,<sup>2</sup> Jianguo Niu,<sup>3</sup> J. Adam Kankiewicz,<sup>4</sup> and Lawrence D. Carey<sup>5</sup>

Received 25 November 2008; revised 3 February 2009; accepted 16 April 2009; published 30 June 2009.

[1] This paper uses a numerical model to investigate microphysical, radiative, and dynamical processes in mixed-phase altostratocumulus clouds. Three cloud cases are chosen for study, each of which was observed by aircraft during the fifth or ninth Complex Layered Cloud Experiment (CLEX). These three clouds are numerically modeled using large-eddy simulation (LES). The observed and modeled clouds consist of a mixed-phase layer with a quasi-adiabatic profile of liquid, and a virga layer below that consists of snow. A budget of cloud (liquid) water mixing ratio is constructed from the simulations. It shows that large-scale ascent/descent, radiative cooling/heating, turbulent transport, and microphysical processes are all significant. Liquid is depleted indirectly via depositional growth of snow (the Bergeron-Findeisen process). This process is more influential than depletion of liquid via accretional growth of snow. Also constructed is a budget of snow mixing ratio, which turns out to be somewhat simpler. It shows that snow grows by deposition in and below the liquid (mixed-phase) layer, and sublimates in the remainder of the virga region below. The deposition and sublimation are balanced primarily by sedimentation, which transports the snow from the growth region to the sublimation region below. In our three clouds, the vertical extent of the virga layer is influenced more by the profile of saturation ratio below the liquid (mixed-phase) layer than by the mixing ratio of snow at the top of the virga layer.

**Citation:** Smith, A. J., V. E. Larson, J. Niu, J. A. Kankiewicz, and L. D. Carey (2009), Processes that generate and deplete liquid water and snow in thin midlevel mixed-phase clouds, *J. Geophys. Res.*, 114, D12203, doi:10.1029/2008JD011531.

### 1. Introduction

[2] Altostratocumulus (ASc) clouds are analogous to low-level stratocumulus (Sc), except that ASc occur in midlevels of the troposphere [Larson *et al.*, 2006]. Like Sc, ASc are thin (typically several hundred meters or less), are nearly or entirely overcast (e.g., have a cloud fraction of nearly 1), and have a “bumpy” appearance caused by turbulence that is usually driven in part by radiative cooling and/or heating. Several observational studies have been completed [see, e.g., Hobbs and Rangno, 1985; Gedzelman, 1988; Heymsfield *et al.*, 1991; Larson *et al.*, 2001; Fleishauer *et al.*, 2002; Wang *et al.*, 2004; Carey *et al.*, 2008; Niu *et al.*, 2008]. Unlike Sc, ASc are decoupled from surface fluxes of sensible and latent heat, and are often cold enough to contain ice [Fleishauer *et al.*, 2002]. (We follow the nomencla-

ture of Larson *et al.* [2006], Falk and Larson [2007], and Larson *et al.* [2007] by using “altostratocumulus” to denote overcast altocumulus. We reserve “altocumulus” to denote partly cloudy altocumulus and “altostratus” to denote thicker, more uniform cloud layers. This draws an implicit parallel between midlevel cloud types and boundary layer stratocumulus, cumulus, and stratus cloud types.)

[3] ASc are of practical importance for several reasons. We mention two. First, ASc perturb radiative fluxes at the ground surface. ASc can increase downwelling longwave radiation [Garrett and Zhao, 2006] and decrease downwelling shortwave radiation below cloud. Therefore, an increase in ASc prevalence, all else being equal, would be expected to decrease downwelling shortwave radiation during the day and thereby moderate the diurnal cycle of radiation at the ground. This moderation of the diurnal cycle would occur even if the net cloud radiative forcing of the ASc were zero. The magnitude of shortwave radiation perturbation at the ground is strongly influenced by the fraction of cloud that is liquid rather than ice [Sun and Shine, 1994; Field *et al.*, 2004; Sassen and Khvorostyanov, 2007; Carey *et al.*, 2008]. Second, ASc can be an aircraft icing threat, if and only if significant amounts of supercooled liquid are present. Icing is particularly hazardous for small aircraft such as unmanned aerial vehicles (UAVs). Small UAVs are becoming increasingly popular for both

<sup>1</sup>School of Meteorology, University of Oklahoma, Norman, Oklahoma, USA.

<sup>2</sup>Department of Mathematical Sciences, University of Wisconsin-Milwaukee, Milwaukee, Wisconsin, USA.

<sup>3</sup>IMSG, Center for Satellite Applications and Research, NESDIS, NOAA, Camp Springs, Maryland, USA.

<sup>4</sup>WindLogics, Inc., St. Paul, Minnesota, USA.

<sup>5</sup>Earth System Sciences Center, National Space Science and Technology Center, University of Alabama in Huntsville, Huntsville, Alabama, USA.

civilian and military surveillance, but they have suffered several accidents caused by icing. For instance, owing to icing and bad weather conditions, at least three Predator UAVs crashed in Afghanistan between October 2001 and February 2002 during U.S. military operations there [Haulman, 2003].

[4] Although accurate forecasts of AS<sub>c</sub> would be of practical value, current large-scale models handle midlevel clouds poorly. For instance, in a study of 10 general circulation models, Zhang *et al.* [2005] found that all climate models grossly underpredicted (thin) AS<sub>c</sub> and overpredicted (thick) nimbostratus, relative to satellite observations. (Similar biases occurred for boundary layer clouds.) Similarly, Illingworth *et al.* [2007, Figure 5a] studied seven weather forecast models and found that 6 of them underpredicted cloud fraction in the midlevels.

[5] Because radiative transfer and icing severity depend sensitively on the presence and amount of liquid, this paper will explore what processes generate and deplete liquid, either directly or indirectly. The processes include dynamical ones such as large-scale ascent/descent and small-scale turbulence. They also include physical processes such as radiative cooling/heating, and growth of snow via deposition or accretion. Indirect depletion of liquid by growth of snow is of special interest, and therefore we will investigate further the processes that generate and deplete snow itself. (We distinguish large ice particles of any origin, which we denote “snow,” from small ice particles, which we denote “cloud ice.”)

[6] To investigate these processes, we perform high-resolution, three-dimensional, dynamical simulations. AS<sub>c</sub> clouds have been simulated previously in two spatial dimensions [Starr and Cox, 1985; Liu and Krueger, 1998; Marsham *et al.*, 2006; Sassen and Khvorostyanov, 2007] and three dimensions with a rudimentary microphysical scheme [Larson *et al.*, 2006]. We will simulate three thin, mixed-phase AS<sub>c</sub> clouds that were observed during the fifth and ninth Complex Layered Cloud Experiments (CLEX-5 and CLEX-9).

[7] To investigate processes that influence liquid, we construct a budget of cloud (liquid) water mixing ratio. This budget allows us to quantify and compare the signs and magnitudes of all processes that alter cloud water in our simulations. Additionally, to investigate snow processes, we construct a budget of snow mixing ratio. We find that for our three cases, cloud water is influenced significantly by large-scale ascent or descent, small-scale turbulence, radiative heating and cooling, and depositional growth of snow. However, snow processes are somewhat simpler, with a balance mainly between deposition or sublimation, and sedimentation of snow. Although prior authors have constructed budgets of snow for thick precipitating clouds [Misra *et al.*, 2000; Colle and Zeng, 2004; Colle *et al.*, 2005], to our knowledge, we construct the first complete snow budgets for AS<sub>c</sub>.

[8] An outline of this paper is as follows. In order to put our results in a broader context, section 2 compares and contrasts AS<sub>c</sub> with other, similar cloud types. Section 3 summarizes the observed character of the three cloud cases that we will simulate later. Section 4 describes the large-eddy model that we will use to perform the simulations. Section 5 compares observed and simulated profiles after

model spin-up. Section 6 presents a series of results: the first subsection explores the time evolution of cloud water and snow in the three cases; the next presents budgets of cloud water; the next presents budgets of snow; the next comments on the liquid-over-snow structure found in our clouds, and why it occurs; and the final subsection discusses simulated properties of the snow virga layer below cloud. Section 7 presents conclusions.

## 2. Background: Similarities and Differences Between Midlatitude AS<sub>c</sub> and Other Cloud Types

[9] Here we pause to compare and contrast midlatitude AS<sub>c</sub> with other types of layer clouds. Layer clouds are a vast subject, so our review must necessarily be incomplete.

[10] First, AS<sub>c</sub> have similarities and differences to low-level, marine stratocumulus (Sc). Both cloud types are thin and overcast. Therefore, both experience cloud-top radiative cooling, which generates turbulence that extends below cloud base and also entrains dry air from above cloud top. However, AS<sub>c</sub> reside far above the ground or ocean surface, while the turbulence in Sc typically reaches the surface and permits Sc to be sustained by surface fluxes. Turbulent layers associated with AS<sub>c</sub> entrain *below*-cloud air with different properties [Liu and Krueger, 1998], while often Sc-topped layers are well mixed down to the surface. AS<sub>c</sub> often drift with the mean wind and do not have strong jumps in wind at cloud top [Fleishauer *et al.*, 2002], while Sc often have strong cloud-top shear that is associated with the well-mixedness of Sc within and below cloud and the strong connection of Sc to the surface via turbulence [e.g., Brost *et al.*, 1982]. AS<sub>c</sub> often have moderate to weak cloud-top inversions ( $\leq 5$  K) [Fleishauer *et al.*, 2002], while marine Sc often have stronger inversions ( $\geq 7$  K) [e.g., Schubert *et al.*, 1979; Stevens *et al.*, 2003; Ackerman *et al.*, 2009]. Finally, of course, AS<sub>c</sub> are often mixed-phase, while Sc are often warmer than freezing and in such cases cannot contain ice.

[11] Second, AS<sub>c</sub> also have similarities to low-level mixed-phase Arctic layer clouds. Such clouds have been studied observationally by numerous authors [Pinto, 1998; Hobbs and Rangno, 1998; Pinto *et al.*, 2001; Lawson *et al.*, 2001; McFarquhar *et al.*, 2007; Verlinde *et al.*, 2007]. They have also been simulated by large-scale numerical models [Walsh *et al.*, 2002; Kattsov and Källén, 2005; Rinke *et al.*, 2006; Prenni *et al.*, 2007; Morrison *et al.*, 2008] and fine-scale models [Harrington *et al.*, 1999; Jiang *et al.*, 2000; Olsson and Harrington, 2000; Harrington and Olsson, 2001; Fridlind *et al.*, 2007; Klein *et al.*, 2009]. Like typical AS<sub>c</sub>, low-level Arctic clouds often are thin, overcast, and have radiatively generated turbulence [e.g., Harrington *et al.*, 1999]. Both clouds often have similar mixed-phase microphysics.

[12] However, despite their similar appearance, midlatitude AS<sub>c</sub> clouds and Arctic low clouds have different forcings. For instance, as mentioned before, AS<sub>c</sub> are too high to be influenced significantly by surface fluxes, whereas surface fluxes can be large for Arctic clouds that advect over relatively warm ocean surfaces [Olsson and Harrington, 2000; Harrington and Olsson, 2001; Klein *et al.*, 2009]. (On the other hand, Arctic clouds that reside over an ice

**Table 1.** Approximate Values of Overall Characteristics of the Three Cloud Cases<sup>a</sup>

	Nov 11 Cloud	Oct 14 Cloud	Nov 02 Cloud
Observed cloud top	0.4	0.25	0.15
cloud water mixing ratio $r_c$ ( $\text{g kg}^{-1}$ )			
Mean observed snow mixing ratio $r_S$ ( $\text{g kg}^{-1}$ )	0.02	0.04	0.005
Liquid cloud thickness (m)	500	700	400
Virga thickness (m)	1700	2300	1600
Total cloud system thickness (m)	2200	3000	2000
Initial liquid cloud top altitude, MSL (m)	5700	5300	4700
Liquid cloud top temperature ( $^{\circ}\text{C}$ )	-16	-22	-13
Liquid cloud top pressure (hPa)	500	525	575
Large-scale vertical velocity ( $\text{cm s}^{-1}$ )	-3.0	1.4	0.7

<sup>a</sup>These are derived from aircraft observations where possible and model simulations where necessary.

surface may experience small surface fluxes.) A second difference between midlatitude and Arctic clouds is that Arctic clouds experience weaker diurnal variation of solar radiation [Fleishauer *et al.*, 2002]. The diurnal cycle in solar radiation, in turn, has been hypothesized by Liu and Krueger [1998] and Lazarus *et al.* [2000] to influence diurnal variations in ASc cloudiness. The weaker diurnal forcing is also experienced by *midlevel* Arctic clouds. These clouds have been observed by, for example, Curry [1986], Hobbs and Rangno [1998], Hobbs *et al.* [2001], Pinto *et al.* [2001], and Verlinde *et al.* [2007].

[13] Third, there are several midlatitude, midlevel cloud types that are thicker than ASc, such as altostratus and nimbostratus. Often these clouds are associated with fronts. They have been observed by, for example, Rauber and Tokay [1991], Field [1999], Cober *et al.* [2001b, 2001a], Korolev *et al.* [2003], Field *et al.* [2004], and Korolev *et al.* [2007]. They have been modeled by, for example, Katzfey and Ryan [2000], Ryan *et al.* [2000], Weaver *et al.* [2005], Xu *et al.* [2005], and Clark *et al.* [2005]. The thicker midlevel clouds tend to have greater ice water contents, but not necessarily greater liquid water contents [Korolev *et al.*, 2003; Field *et al.*, 2004; Clark *et al.*, 2005; Korolev *et al.*, 2007].

### 3. The Three Cloud Cases

[14] The three cloud cases that we study here were all observed by aircraft, and all are simulated by a large-eddy model. The cases are named according to the date on which they were observed: Nov 11, Oct 14, and Nov 02.

[15] All three cases share certain characteristics. They are all thin, single-layer, mixed-phase, ASc cloud systems consisting of a predominantly liquid layer atop a snow virga layer below. (In the sequel, we will refer to this mixed-phase but predominantly liquid layer as the “liquid (mixed-phase) layer.” In our cases, no liquid occurs outside this layer.) However, they differ in detail, as outlined in Table 1. Table 1 contains approximate numbers gleaned from aircraft observations where available. However, the

virga thickness and total cloud system thickness are obtained from the simulations we describe below, and the large-scale vertical velocity is obtained for the Nov 11 case from Larson *et al.* [2006] and for the Oct 14 and Nov 02 cases from the National Centers for Environmental Prediction (NCEP) North American Regional Reanalysis (NARR).

[16] Table 1 highlights some key differences and similarities. The Nov 11 case undergoes large-scale descent ( $-3 \text{ cm s}^{-1}$ ), whereas the Oct 14 and Nov 02 cases undergo ascent ( $1.4$  and  $0.7 \text{ cm s}^{-1}$ , respectively). The layers containing liquid are thin, ranging from 400 to 700 m, but the overall thickness including virga ranges from 2000 to 3000 m. The cloud-top temperatures permit mixed-phase conditions and vary from  $-22^{\circ}\text{C}$  to  $-13^{\circ}\text{C}$ . The snow (ice) mixing ratios are small, ranging from  $r_S = 0.005$  to  $0.04 \text{ g kg}^{-1}$ , with more snow present in the colder clouds. The cloud-top cloud water mixing ratios vary from  $r_c = 0.15$  to  $0.4 \text{ g kg}^{-1}$ , and show no trend with temperature.

[17] We now summarize background information for each case. We will be brief, because observations of the Nov 11 case are presented by Fleishauer *et al.* [2002], and observations of the Oct 14 and Nov 02 cases are presented by Carey *et al.* [2008].

#### 3.1. Nov 11 Cloud

[18] The Nov 11 cloud was sampled by an aircraft over central Montana on 11 November 1999 during the fifth of the Complex Layered-Cloud Experiments (CLEX-5). One spiral sounding was performed in the layer, along with a series of aircraft legs to measure horizontal variability. Descriptions of the aircraft, instrumentation and observations are provided by Fleishauer *et al.* [2002].

[19] The Nov 11 cloud system was the subject of a three-dimensional LES study by Larson *et al.* [2006]. In that study, a highly idealized ice parameterization was used to simulate depositional growth of ice, because the authors wished to study effects on only the liquid portion of the cloud. In the present study, we use a more sophisticated single-moment scheme, described below.

[20] We also simulate two cloud systems sampled during the ninth of the Complex Layered-Cloud Experiments (CLEX-9). These are described in sections 3.2 and 3.3.

#### 3.2. Oct 14 Cloud

[21] One CLEX-9 cloud system was observed on 14 October 2001 near North Platte, Nebraska [Carey *et al.*, 2008; J. A. Kankiewicz *et al.*, The morphology of two mixed phase clouds, paper presented at 11th Conference on Cloud Physics, American Meteorological Society, Ogden, Utah, 2002]. The cloud field formed before sunrise, and the aircraft sampled the region between 1210 and 1600 UTC. A second sampling period was performed from 1715 to 1900 UTC, indicating that the cloud field persisted for a significant length of time.

[22] The Oct 14 cloud was sampled with the University of Wyoming’s King Air aircraft. Instruments used during the sampling included two-dimensional cloud (2D-C) and two-dimensional precipitation (2D-P) probes for measuring the size distribution of ice and snow particles, forward scattering spectrometer probe (FSSP) for small particles, upward- and side-looking Wyoming Cloud Radar, and probes to measure the thermodynamic and aircraft geographic location. A

spiral sounding and two leg soundings were completed. For more information on the aircraft instrumentation and methodology, refer to *Carey et al.* [2008] or *Niu et al.* [2008].

[23] In this cloud case, in situ sampling was limited to the liquid (mixed-phase) layer and part of the corresponding snow virga. The aircraft did not perform sampling below 3000 m, and hence the complete virga layer thickness cannot be determined. An additional sounding was obtained from a special rawinsonde launched during the aircraft flight. The rawinsonde was launched from the National Weather Service's North Platte, Nebraska, office, located at the Lee Bird Field (LBF) airport, which is approximately 72 km from the aircraft sampling region.

[24] The cloud field was embedded in large-scale ascent. A value of  $1.4 \text{ cm s}^{-1}$  was determined using data from the National Centers for Environmental Prediction (NCEP) North American Regional Reanalysis (NARR). The times selected for this data were 1200 UTC and 1500 UTC on 14 October 2001.

### 3.3. Nov 02 Cloud

[25] The third cloud case that we study was observed on 02 November 2001 during the CLEX-9 experiment [*Carey et al.*, 2008; *Kankiewicz et al.*, presented paper, 2002]. This region was sampled by aircraft between 1220 UTC and 1620 UTC. After 1600 UTC, the cloud field began to dissipate, with complete evaporation occurring by 1730 UTC. The Nov 02 cloud top temperature was nearly  $-13^\circ\text{C}$ , which is  $9^\circ$  warmer than the Oct 14 cloud.

[26] Aircraft observations indicate a snow virga layer that extends as much as 250 m below the liquid (mixed-phase) layer. However, the aircraft did not sample below 4200 m. Additional cloud lidar observations (*L. D. Carey et al.*, MM-wave radar structure and microphysical characteristics of a mixed-phase altocumulus cloud on 2 November 2001, Figure 2, paper presented at 32nd Conference on Radar Meteorology, Albuquerque, New Mexico, American Meteorological Society, 2005) indicate that the virga may have extended as far as 600 m below the liquid (mixed-phase) layer. However, the exact extent of the snow virga layer cannot be determined from our data.

[27] Because the Nov 02 cloud was observed as part of the CLEX-9 experiment, the aircraft instruments and sampling methods are the same as for the Oct 14 case. To obtain thermodynamic data above and below the cloud region, we again use a supplemental sounding launched from LBF during the observation period. Like the Oct 14 case, the Nov 02 case was sampled approximately 72 km from the LBF site.

## 4. Description of the Large-Eddy Simulation Model, COAMPS-LES

### 4.1. Model Configuration

[28] To simulate the aforementioned three clouds, we use the Coupled Ocean/Atmosphere Mesoscale Prediction System (COAMPS<sup>®</sup>) Large-Eddy Simulation (COAMPS-LES) model [*Golaz et al.*, 2005]. In prior studies, this model has successfully simulated observed boundary layer clouds [*Golaz et al.*, 2005] and observed altostratocumulus clouds [*Larson et al.*, 2006; *Falk and Larson*, 2007]. An overview

of the model is available from *Hodur* [1997]. For modelers who wish to reproduce our simulations, a detailed specification of our case configurations is contained in the auxiliary material.<sup>1</sup>

[29] All of our simulations are three dimensional with fine grid spacing and a small time step. All simulations use a horizontal grid spacing of  $75 \text{ m} \times 75 \text{ m}$  and a vertical grid spacing of 25 m. The horizontal domain size is  $4125 \text{ m} \times 4125 \text{ m}$ . We use a different vertical domain size for each case because each cloud system has a different thickness. The vertical domain spans 4400 m for the Nov 11 case, 4500 m for the Oct 14 case, and 3000 m for the Nov 02 case. This is large enough to allow the virga to sublimate entirely before reaching the domain base. Because all cloud systems are isolated from the boundary layer, surface and momentum fluxes at the lower model boundary are set to zero. The time step is 1 s, with a total simulated time of 4 h for each case.

[30] Our simulations use the anelastic approximation, which accounts for vertical variation in air density in the model basic state. The simulations use periodic boundary conditions in the horizontal and are initialized with a horizontally uniform profile. Therefore, the simulations cannot account for large-scale horizontal trends. To set up horizontal wind profiles in our simulations, we obtain the aircraft-observed wind profile in both horizontal directions, and then subtract the time- and domain-average wind in order to produce a wind profile relative to cloud motion. This maximizes the time step that we can use without incurring numerical instability.

[31] We apply large-scale ascent or descent to individual simulations by selecting a constant velocity and using it to vertically advect water vapor, potential temperature and horizontal winds. The values of ascent or descent are provided in the individual cloud case descriptions above.

[32] To allow turbulence and radiation to come into equilibrium, a 1-h spin-up period is completed before any microphysics is switched on. We ensure that after this initial spin-up period without microphysics, our simulated clouds closely match actual conditions at the time of aircraft observations (see below). One hour after the simulation has begun, microphysics is activated, and an additional spin-up period of 30 min is applied in order to allow ice and snow to form and approach equilibrium.

### 4.2. Radiative Schemes

[33] Longwave radiation is calculated using the method and parameter values listed by *Larson et al.* [2007]. Shortwave radiation is calculated using the two-stream, single-band model of *Shettle and Weinman* [1970] and *Duynkerke et al.* [2004]. Cosine of the solar zenith angle is allowed to vary in the Oct 14 and Nov 02 cases, but is simply set to  $\approx 0.43$  in the Nov 11 case, because this cloud lasted only 74 min (even though the Nov 11 *simulation* lasted 4 h). The aforementioned radiation models account for liquid but not snow or water vapor. The neglect of snow is acceptable because the mixing ratio of snow is about 10 times smaller than the mixing ratio of liquid in our simulations, and because radiation is used primarily to generate turbulence.

<sup>1</sup>Auxiliary materials are available in the HTML. doi:10.1029/2008JD011531.

Furthermore, our calculations assume that snow has the same temperature as cloud water, water vapor, and dry air. In nature, the temperature of snow may be different because of direct radiative cooling or heating of snow crystals. *Lebo et al.* [2008] have found that this effect may change typical glaciation rates by 5% to 15% [see also *Marquis and Harrington*, 2005]. The neglect of water vapor is acceptable since our simulations last 4 h, and on such short time scales, radiation does not greatly influence air temperature.

### 4.3. Single-Moment Microphysical Scheme

[34] COAMPS-LES uses a single-moment bulk microphysical scheme based on the widely used formulation of *Rutledge and Hobbs* [1983]. Detailed information on the microphysical equations is given by *Long* [2003]. The scheme prognoses the mixing ratios of five hydrometeor species: cloud water ( $r_c$ ), rain ( $r_r$ ), cloud ice ( $r_i$ ), snow ( $r_s$ ), and graupel ( $r_g$ ). The scheme is single moment, and therefore diagnoses number concentrations rather than prognoses them. The model distinguishes between cloud ice and snow: snow sediments, but cloud ice does not. A cloud ice particle is converted to a snow crystal when it becomes large enough. In all of our cloud cases, aircraft observations show no evidence of graupel, so we deactivate graupel processes in our simulations.

[35] The *Rutledge and Hobbs* [1983] scheme includes representations of cloud ice nucleation, depositional growth, collection of cloud droplets by snow, and sedimentation of snow. In our simulations, we calculate ice particle number concentration using formulas from *Fletcher* [1962] and *Cooper* [1986]. At each grid point where microphysics is applied, the ice number concentration is diagnosed from each formula, and the larger concentration is used. We have tested alternative ice nucleation formulas, such as the *Meyers et al.* [1992] and the *Fletcher and Cooper* formulas used individually rather than in conjunction with each other. These tests indicated that the combined *Fletcher/Cooper* method generates the most accurate snow conditions for our study.

[36] The *Fletcher/Cooper* method is simple, but it has several drawbacks. For instance, it calculates ice number concentration as a diagnostic function of temperature alone. Because the concentration is determined diagnostically rather than by transport equations, the *Fletcher/Cooper* method implicitly neglects the sink of ice nuclei that occurs when snow sediments out of the cloud layer. Because of this lack of generality, we were forced to multiply the *Fletcher and Cooper* formulas by a coefficient equal to 0.06 in order to produce realistic results in the Oct 14 case, perhaps because the *Fletcher/Cooper* formula produces excessive ice nuclei concentrations in colder clouds such as the Oct 14 cloud, or perhaps because the Oct 14 air mass contained anomalously few ice nuclei. Without the factor of 0.06, too much snow was generated in the simulation, and liquid was depleted too rapidly. Such ad hoc adjustments are undesirable. However, we have no ice nuclei measurements against which to check the values we used.

[37] The *Rutledge-Hobbs* scheme assumes an exponential snow size distribution, which was observed to be approximately true for the Oct 14 cloud for snow particles of diameter greater than 600 microns [*Niu et al.*, 2008]. The *Rutledge-Hobbs* exponential size distribution contains a

snow intercept parameter,  $N_{0S}$ . The value of  $N_{0S}$  that we use in our numerical simulations ( $2 \times 10^7 \text{ m}^{-4}$ ) straddles the values observed in the Nov 11 cloud (about  $10^8 \text{ m}^{-4}$  [*Fleishauer et al.*, 2002]) and in the Oct 14 cloud ( $10^6$  to  $10^7 \text{ m}^{-4}$  [*Niu et al.*, 2008]).

[38] The *Rutledge-Hobbs* scheme is a single-moment scheme, and as such, it cannot represent aggregation. On the basis of inspection of images from a 2D-C probe for the Oct 14 and Nov 02 cases, *Niu et al.* [2008] and *Carey et al.* [2008] suggested that some aggregates did exist. In the Nov 11 case, images from a higher-resolution Cloud Particle Imager probe suggest that the snow crystals in that case are more likely depositionally grown polycrystals rather than aggregates.

[39] The single-moment microphysics scheme that we use is computationally inexpensive, relatively simple to interpret, and sufficiently accurate for this first broad-brush effort. However, it would be of interest to repeat the calculations with a more sophisticated methodology, such as a double-moment bulk microphysics scheme [e.g., *Ferrier*, 1994; *Morrison et al.*, 2005] or bin microphysical scheme [e.g., *Reisin et al.*, 1996; *Lynn et al.*, 2005].

## 5. Comparison of Simulated Profiles to Aircraft Observations

[40] In order to investigate processes that generate and deplete liquid water and snow, we will analyze budgets constructed from simulations. We cannot verify the simulated budget terms by direct observations. Neither can we directly verify the mass-diameter and fallspeed-diameter relationships used in our numerical model. However, the observations can be used to test the simulated liquid and snow profiles. While this does not tightly constrain the simulated budgets, it does provide evidence that the simulated clouds are plausible and realistic.

### 5.1. Set-Up of Initial Profiles

[41] We now verify that the simulated nonmicrophysical fields match aircraft observations at the initial time. Here, the simulated “initial” profiles refer to the 61st minute, which immediately follows the first 1-h spin-up period.

[42] The Nov 11 cloud case is shown in Figure 1. Cloud water mixing ratio ( $r_c$ ) is examined in Figure 1a, water vapor mixing ratio ( $r_v$ ) in Figure 1b, and potential temperature ( $\theta$ ) in Figure 1c. For all three variables, we display the mean vertical profile of the simulated variable (solid line) along with the corresponding aircraft spiral sounding (crosses). All simulated profiles are horizontally averaged over the model domain. Each plot shows that the simulation produces a reasonable profile of temperature and moisture.

[43] Similarly, we also examine the moisture and temperature profiles for the Oct 14 (Figure 2) and Nov 02 (Figure 3) cloud cases. For each of these cases, three aircraft soundings were available, and each sounding showed variation in the magnitude and vertical extent of liquid. To demonstrate that our simulated  $r_c$  profiles are initialized suitably, we display simulated  $r_c$  (Figure 2a, solid line) along with all aircraft observations (indicated by crosses, dots and triangles). Furthermore, our simulated profiles of potential temperature ( $\theta$ ) adequately match the aircraft and rawinsonde observations (Figures 2c and 3c).

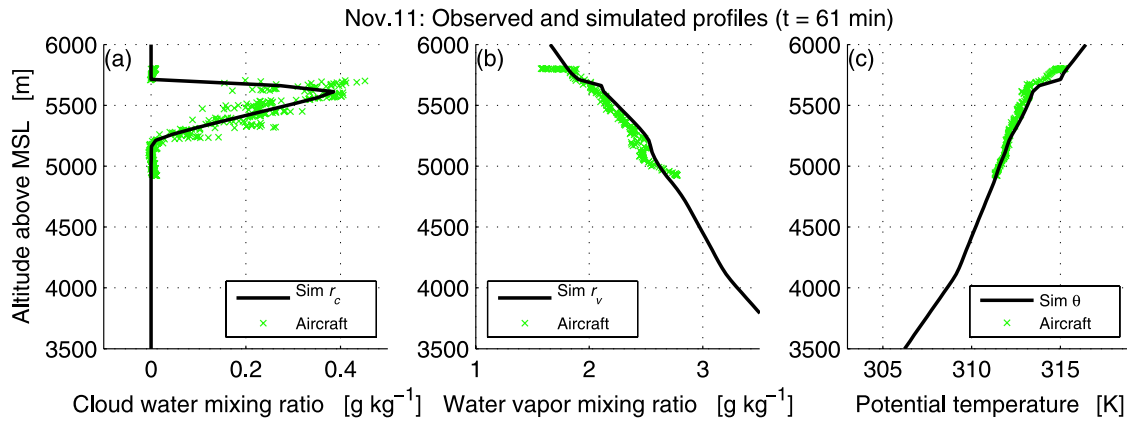


**Figure 1.** A comparison of simulated profiles from the Nov 11 cloud case at  $t = 61$  min (solid line) versus the available aircraft sounding (crosses). The simulated profiles are obtained immediately after the primary model spin-up period is completed. Profiles displayed are (a) cloud water mixing ratio ( $r_c$ ), (b) water vapor mixing ratio ( $r_v$ ), and (c) potential temperature ( $\theta$ ). The good fit verifies that the model has been initialized with the correct profiles.

[44] Unfortunately, if we assume that  $\theta$  and  $r_c$  are accurately measured, then we cannot match the aircraft-observed profile of  $r_v$  because it is inconsistent with  $\theta$  and  $r_c$ . In particular, the aircraft-observed value of  $r_v$  greatly exceeds saturation with respect to liquid within cloud, rather than being exactly saturated, as expected. This is illustrated in Figure 2b for the Oct 14 cloud and Figure 3b for the Nov 02 cloud. However, the supplemental soundings from LBF (dashed lines) do indicate that  $r_v$  nearly equals the saturation mixing ratio within cloud. Therefore, we use a  $r_v$  profile that more closely follows the supplemental sounding profile.

**5.2. Tests of Snow Profiles**

[45] As a first test of our simulations, Figure 4 examines the accuracy of snow mixing ratio. The profile of snow mixing ratio ( $r_s$ ) is plotted 30 min after the “initial” (61st-minute) time, in order to allow the microphysics to

equilibrate. Because the snow profile at this time step is relatively unconstrained, this provides a nontrivial test of our model’s fidelity to observations. Figure 4 displays the simulated mean profile of  $r_s$  (solid line) and the mean plus or minus 1 standard deviation (thin lines), the aircraft spiral sounding (crosses), and  $r_s$  from three separate aircraft legs (dots, asterisks, and triangles).

[46] Figure 4 (top) shows the Nov 11 case. For this case, no aircraft data are available below 4800 m, and hence we cannot test the model values below this altitude. Above 4800 m, however, the plot indicates that the model produces a reasonable mean snow profile. Additionally, Larson et al. [2006] showed that the simulated turbulence profile and cloud lifetime for the Nov 11 case compare satisfactorily with observations.

[47] The Oct 14 simulation (Figure 4, middle) appears to accurately represent the depth of the snow layer but

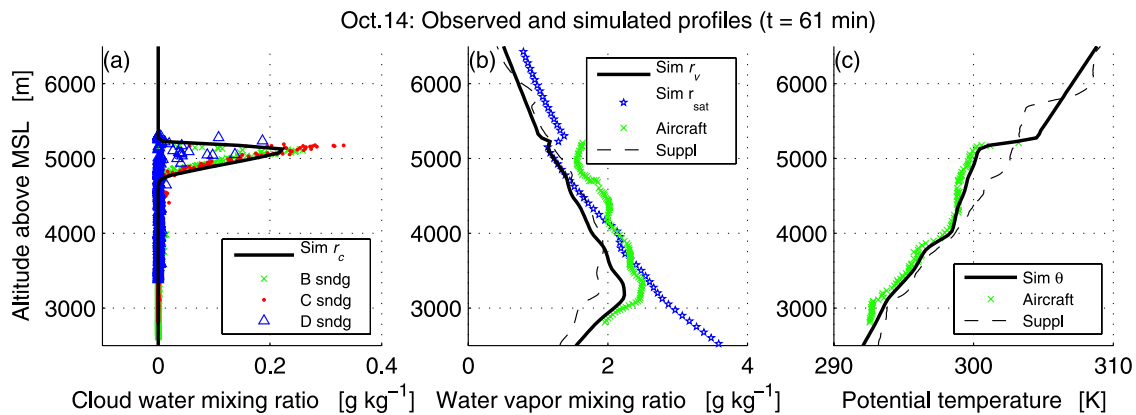


**Figure 2.** A comparison of simulated profiles from the Oct 14 cloud case at  $t = 61$  min (solid lines) versus the available aircraft and supplemental soundings. (a) Three aircraft soundings are included, represented by crosses, dots, and triangles. (b and c) Simulated profiles are compared with observations obtained by aircraft (crosses) and the rawinsonde launched from station LBF (dashed lines). For reference, Figure 2b also includes the simulated saturation mixing ratio with respect to liquid (stars). This shows that if we match aircraft-observed  $\theta$  and  $r_c$ , we cannot also match  $r_v$ , indicating an inconsistency in the observations.

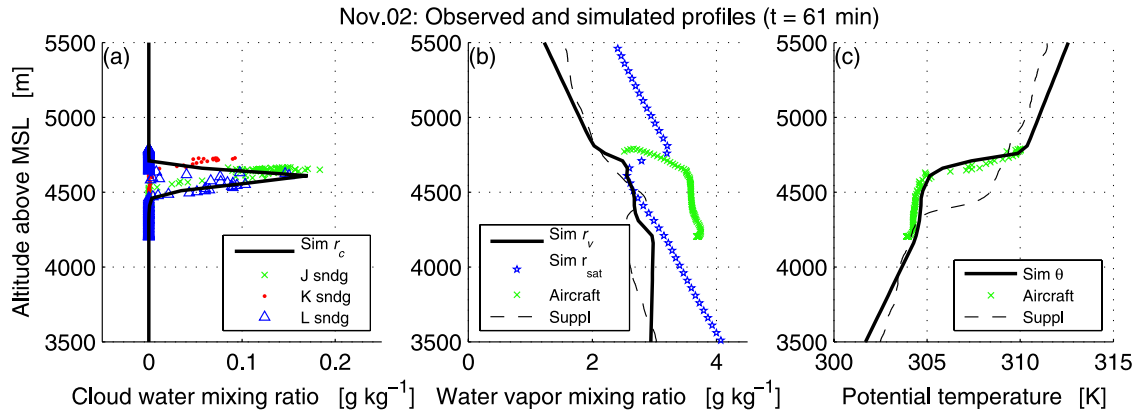


**Figure 3.** A comparison of simulated profiles from the Nov 02 cloud case at  $t = 61$  min (solid lines) versus the available aircraft and supplemental soundings. (a) Three aircraft soundings are included, represented by crosses, dots, and triangles. (b and c) Simulated profiles are compared with observations obtained by aircraft (crosses) and a supplemental rawinsonde sounding (dashed line). For reference, Figure 3b also includes the simulated saturation mixing ratio with respect to liquid (stars). This shows that if we match aircraft-observed  $\theta$  and  $r_c$ , we cannot also match  $r_v$ , indicating an inconsistency in the observations.

underestimates the horizontal standard deviation of  $r_s$ . It is difficult to ascertain whether the underestimation arises from an inaccurate formulation of ice nucleation, other inaccurately modeled physics, or another error.

[48] The Nov 02 simulation (Figure 4, bottom) produces a reasonable profile of  $r_s$  within the mixed-phase cloud region. For this case, the aircraft data does not extend below 4200 m, but the lidar data does indicate the presence of ice up to 600 m below the liquid (mixed-phase) layer. Given this, the simulated results are plausible.

## 6. Results

### 6.1. Time Evolution of Liquid and Snow

[49] The time evolution of profiles of cloud water and snow for each cloud case is displayed in Figure 5. In each plot, cloud water mixing ratio,  $r_c$ , is indicated by the shaded contours, and snow mixing ratio,  $r_s$ , is indicated by the unshaded contours. All plots show data from the initial observation (after the 1-h spin-up period) to the end of the simulation.

[50] In all three cases, cloud water increases quasi-adiabatically with increasing altitude. This is because the liquid (mixed-phase) layers are not strongly depleted by snow and reside in layers that are reasonably well mixed in the vertical by turbulence. In contrast, snow mixing ratio maximizes at or below liquid cloud base. The reason is that snow crystals fall as they grow larger by deposition or accretion [Fleishauer et al., 2002]. These liquid and snow profiles combine to form a mixed-phase layer in which, as altitude increases, liquid increases and snow decreases. This structure of liquid over snow agrees with observational data examined by Rauber and Tokay [1991], Fleishauer et al. [2002], and Carey et al. [2008], but contrasts with simple parameterizations that posit that the fraction of ice increases with decreasing temperature [Smith, 1990; Bower et al., 1996; Khairoutdinov and Randall, 2003; Boudala et al., 2004]. These parameterizations have the potential to produce a reasonable climatological average profile of ice fraction but are not general

enough to work well in individual cases such as the ones we present.

[51] In the Nov 11 case (Figure 5, top), the liquid disappears approximately 150 min after the initial aircraft observation, compared to the observed dissipation time of 134 min [Fleishauer et al., 2002; Larson et al., 2006]. The dissipation of cloud is caused partly by the strong large-scale descent ( $3 \text{ cm s}^{-1}$ ) that occurred [Larson et al., 2001, 2006]. In contrast, both the Oct 14 (Figure 5, middle) and Nov 02 (Figure 5, bottom) clouds persist through the simulation period. These results agree with observations, which indicate that the Oct 14 and Nov 02 cloud fields survive more than 4 h after sampling. The persistence is related to the observed large-scale ascent for these clouds.

[52] In all three cloud cases, cloudy air near cloud top entrains nonturbulent above-cloud air and thereby causes cloud top to rise relative to the large-scale vertical velocity. However, the Nov 11 cloud top sinks with respect to the ground, whereas the Oct 14 and Nov 02 clouds rise. This is because the Nov 11 cloud is embedded in large-scale descent, and the other two clouds are embedded in ascending air.

[53] The liquid cloud base behaves differently; namely, it rises in all three cases. The entrainment process is quite different at liquid cloud base than at cloud top. The liquid portion of the cloud system resides within a turbulent layer that extends some distance below liquid cloud base. Therefore, cloudy air near liquid cloud base does not reside at an interface between turbulent and nonturbulent air, and does not entrain nonturbulent, ambient air from below. Rather, cloud-base air mixes with air from the preexisting turbulent layer below. Independently, the base of the turbulent layer may rise with time [Liu and Krueger, 1998], leading to net detrainment of air from the turbulent layer, rather than entrainment. This complicates the parameterization of such cloud layers.

[54] In all three simulations,  $r_c$  tends to decrease with time. Snow mixing ratio either decreases with time (Nov 11) or stays roughly constant (Oct 14 and Nov 02). At any fixed

altitude, however, the ratio of snow to liquid increases with time. In this sense, the clouds glaciate. Other papers have speculated that clouds can deglaciate, that is, have a ratio of snow to liquid that decreases with time [Carey et al., 2008; Kankiewicz et al., presented paper, 2002]. This might occur,

for instance, if ice nuclei were depleted with time by fallout of snow crystals. Our simulations diagnose the ice nuclei concentration on the basis of temperature, and therefore cannot represent this process.

### 6.2. What Processes Contribute Most to the Generation and Depletion of Cloud Water?

[55] It is the presence or absence of cloud water, rather than snow, that determines whether aircraft icing can occur. Furthermore, the amount of cloud water greatly affects cloud albedo. However, forecasting the amount of liquid is complex partly because the amount of liquid is affected by many physical processes. To compare their relative contributions, we compute within COAMPS-LES the following budget for horizontally averaged cloud water mixing ratio,  $\langle r_c \rangle$ :

$$\frac{\partial \langle r_c \rangle}{\partial t} = \text{Mixing}_{r_c} + \text{Ascent}_{r_c} + \text{Radiation}_{r_c} + \text{Collection}_{r_c} + \text{Snow Deposition}_{r_c} + \text{Ice Deposition}_{r_c}, \quad (1)$$

where  $\text{Mixing}_{r_c}$  is the time rate of change in  $\langle r_c \rangle$  due to turbulent mixing,  $\text{Ascent}_{r_c}$  is the change due to large-scale ascent (or descent),  $\text{Radiation}_{r_c}$  is the indirect change in  $\langle r_c \rangle$  due to radiative heating or cooling,  $\text{Collection}_{r_c}$  is the change in  $\langle r_c \rangle$  due to collection of cloud droplets by falling snow,  $\text{Snow Deposition}_{r_c}$  is the indirect change in  $\langle r_c \rangle$  due to depositional growth of snow and the Bergeron-Findeisen effect, and  $\text{Ice Deposition}_{r_c}$  is the indirect change in  $\langle r_c \rangle$  due to depositional growth of cloud ice.

[56] To simplify the interpretation of this budget, we derive it in terms of the “conserved” variables total water mixing ratio (denoted  $r_t$  and equal to vapor plus cloud water but not snow or ice) and liquid water potential temperature (denoted  $\theta_l$ , which also does not include the effects of ice or snow) [Larson et al., 2006]. The variables  $r_t$  and  $\theta_l$  are conserved in the presence of condensation of vapor and adiabatic lifting, but not precipitation, freezing of liquid, or radiative cooling. In order to diagnose  $r_c$  in terms of  $r_t$  and  $\theta_l$ , the budget assumes that when cloud water is present, air is exactly saturated with respect to liquid and that the cloud is overcast, i.e., has cloud fraction 1. These assumptions are adequately satisfied by our clouds. Two advantages of this “conserved-variable”  $r_c$  budget are that (1) it partitions all condensation and evaporation of  $r_c$  among physical processes rather than leaving a generic condensation/evaporation term in the budget; and (2) it includes radiative transfer’s secondhand effect on  $r_c$ . The

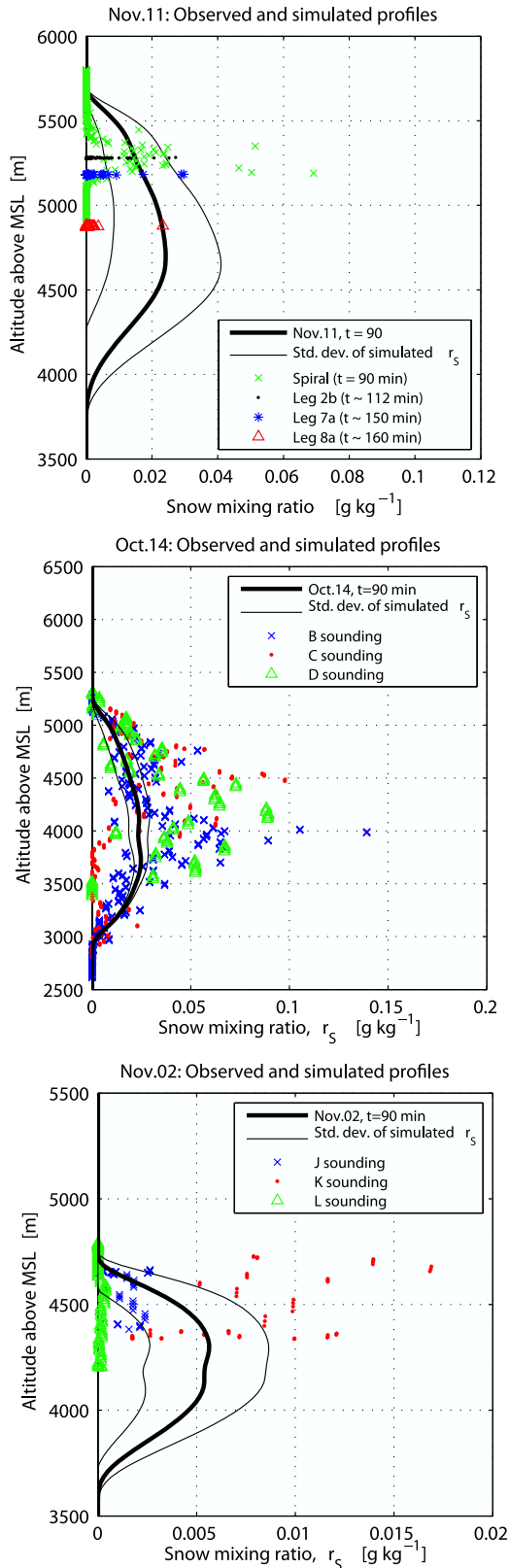
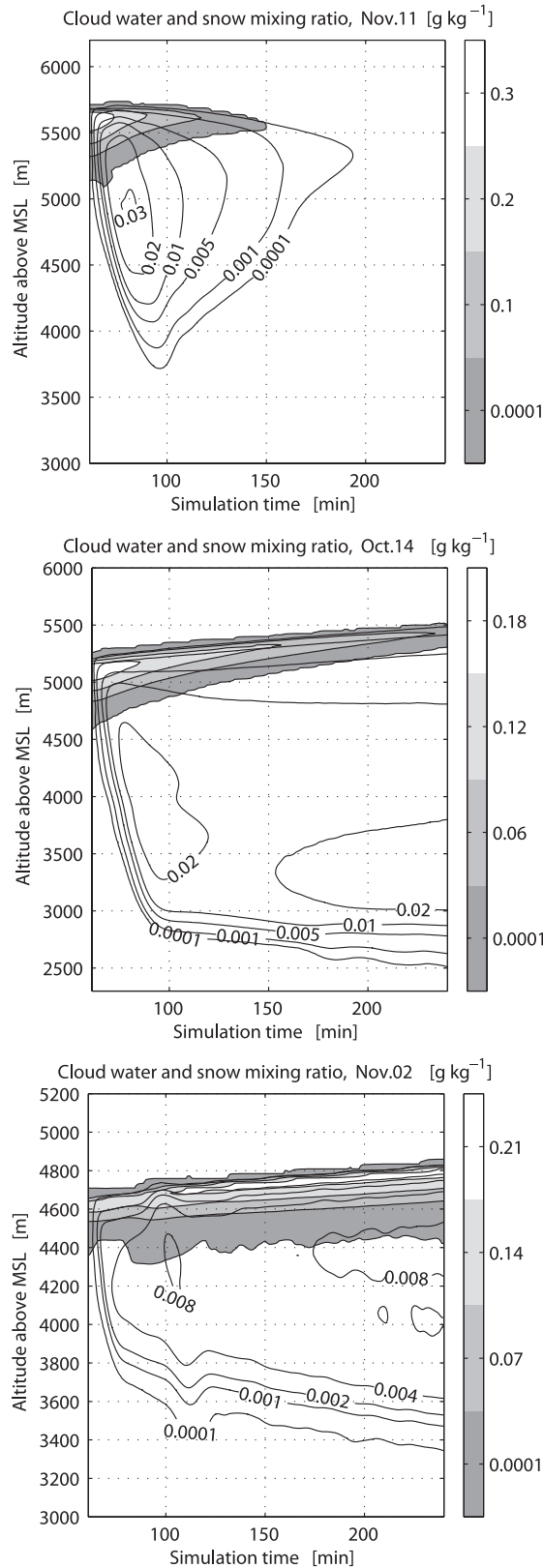


**Figure 4.** Plots at  $t = 90$  min displaying simulated mean  $r_s$  (thick solid line) and the mean plus or minus 1 standard deviation (thin lines). Also shown are aircraft spiral soundings and legs (crosses, dots, asterisks, and triangles). (top) The Nov 11 cloud. No observations are available below 4800 m, but above this level, the model and observations agree. (middle) The Oct 14 cloud. In this case, the model simulates the mean  $r_s$  adequately but underestimates the standard deviation. (bottom) The Nov 02 cloud. The model simulates the mean  $r_s$  adequately above 4200 m; below this altitude there are no observations.

simulated budget does not compute any term as a residual of the others and has been verified to balance.

[57] The  $r_c$  budgets of the three cloud cases are displayed in Figures 6–8. We now compare and contrast these budgets.



[58] In all three cases, the physics terms are qualitatively similar. The radiative profiles (stars) exhibit cooling near cloud top and heating near liquid cloud base. Radiation thereby leads to condensation of liquid near cloud top and evaporation near cloud base. The cloud-top cooling occurs because cloud-top parcels radiate upward but in return receive little compensating radiation from above. The cloud-base warming occurs because the clouds are located at midlevels and therefore are much cooler than the underlying ground. The cloud-base warming offsets much of the cloud-top cooling, leading to less generation of cloud water than one might expect if the cloud were a low cloud. The three microphysical processes that affect  $r_c$ —depositional growth of snow (crosses), collection of cloud droplets by snow (squares), and depositional growth of cloud ice (dots), shown in Figures 6–8—deplete  $r_c$  at all altitudes, as expected. Depositional growth of snow is significantly larger than collection of cloud droplets by snow. This is consistent with the aircraft observations of the CLEX-9 clouds by Carey *et al.* [2008] and Niu *et al.* [2008], which did not reveal much riming or graupel.

[59] The dynamical terms, however, differ between the cloud cases. The Nov 11 cloud experienced large-scale descent (diamonds in Figures 6–8), which led to adiabatic heating and evaporation of cloud water. The Oct 14 and Nov 02 clouds experienced large-scale ascent, which led to condensation. Therefore the large-scale ascent/descent term is negative for the Nov 11 cloud but positive for the other two clouds. This difference leads to a difference in the overall time tendency of  $r_c$  terms (thick solid line in Figures 6–8). Namely, the Nov 11 cloud did not rise with respect to the ground, and suffered depletion of  $r_c$  at all altitudes. On the other hand, the Oct 14 and Nov 02 clouds rose with time, and accordingly generated  $r_c$  above the initial cloud top while depleting  $r_c$  below.

[60] In the Nov 11 cloud, the turbulent mixing term (open circles in Figures 6–8) is small, but in the Oct 14 and Nov 02 clouds this term tends to counteract the time tendency of  $r_c$ , removing  $r_c$  from near cloud top and depositing it below. In all three cases, turbulent mixing creates nearly well-mixed profiles of  $r_i$  and  $\theta_i$ ; therefore, mixing must transport  $r_c$  however needed in order to maintain a quasi-adiabatic profile. Note also that although turbulent mixing has large positive or negative values, its vertical average is small, even though it is not constrained to be zero, as would the turbulent mixing of a conserved variable such as  $r_i$  or  $\theta_i$ . Because its vertical average is small, entrainment of dry air from above does not appear to significantly deplete cloud water in these cases. The reason

**Figure 5.** Time evolution of simulated cloud water mixing ratio ( $r_c$ , shaded contours) and snow mixing ratio ( $r_s$ , unshaded contours). (top) The Nov 11 cloud. It dissipates owing to strong large-scale descent. (middle) The Oct 14 cloud. In this case, snow mixing ratio maximizes far below liquid cloud base because supersaturation with respect to ice also extends far below. (bottom) The Nov 02 cloud. It reaches a quasi-steady state. All three cases show a liquid-over-snow structure, with liquid increasing quasi-adiabatically with height, and snow maximizing at or below liquid cloud base.

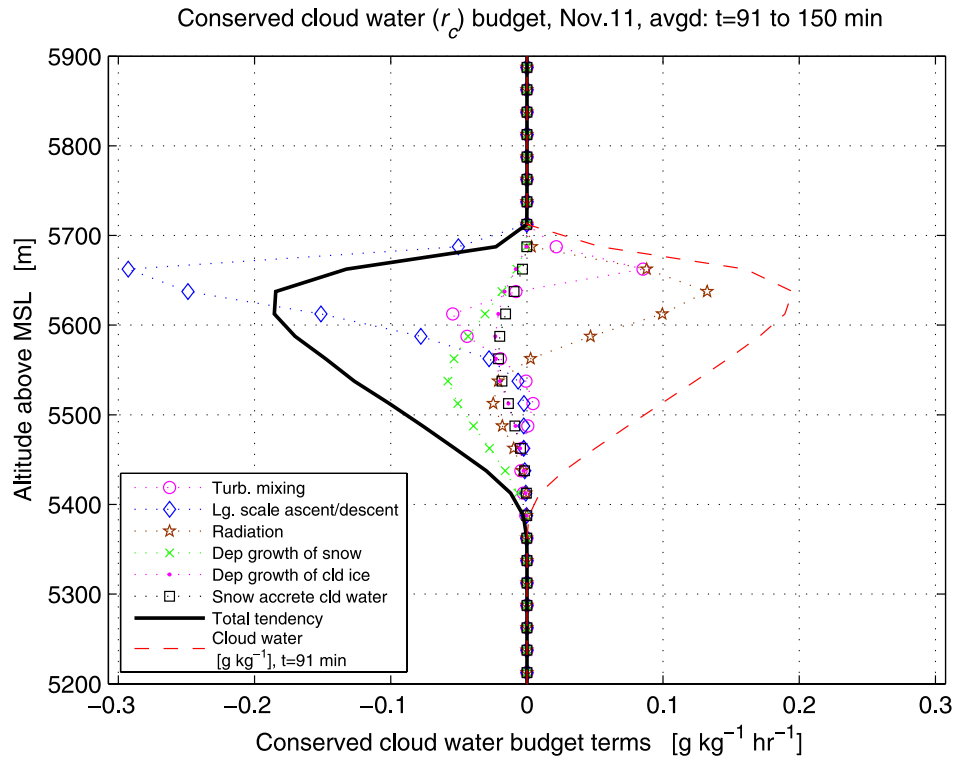


**Figure 6.** A budget of cloud water mixing ratio ( $r_c$ ) for the Nov 11 cloud case, time-averaged from  $t = 91$  to 150 min. Points in the negative region of the plot indicate that liquid is depleted by a process, while points in the positive region indicate that liquid is generated. The overall tendency of  $r_c$  is indicated by the solid line, and individual model processes are indicated by symbols. For reference, a dashed line indicates the cloud water mixing ratio profile at  $t = 91$  min. Large-scale descent, and hence the time tendency, are negative or zero at all altitudes. Depositional growth of snow is stronger than collection of liquid droplets.

may be that the air above cloud cannot be much drier than within-cloud air in cold clouds such as these.

[61] In summary, the terms with the largest vertical average tend to be large-scale ascent or descent, which can either generate or deplete liquid; depositional growth of snow, which always depletes liquid; and radiative transfer, which produces strong cooling near cloud top and weaker heating near cloud base.

### 6.3. What Processes Generate and Deplete Snow?

[62] In section 6.2, we explored how liquid is influenced by various physical processes, including those associated with snow. Now we examine what processes influence the generation and depletion of snow itself.

[63] To do so, we construct budgets of snow mixing ratio. The construction of these snow budgets does not require the assumptions associated with our  $r_c$  budget, namely, those of exact saturation and overcast conditions. The snow budget does not compute any term as a residual of the others, and we have verified that the budget balances.

[64] The budget equation for horizontally averaged snow mixing ratio,  $\langle r_s \rangle$ , may be written as follows:

$$\frac{\partial \langle r_s \rangle}{\partial t} = \text{Mixing}_{r_s} + \text{Sedimentation}_{r_s} + \text{Collection}_{r_s} + \text{Deposition}_{r_s} + \text{Ice Conversion}_{r_s}, \quad (2)$$

where  $\text{Mixing}_{r_s}$  is time rate of change of  $\langle r_s \rangle$  due to turbulent mixing,  $\text{Sedimentation}_{r_s}$  is the change due to fallout of snow,  $\text{Collection}_{r_s}$  is the increase of  $\langle r_s \rangle$  due to collection of cloud water by snow,  $\text{Deposition}_{r_s}$  is change of  $\langle r_s \rangle$  due to deposition or sublimation of water vapor, and  $\text{Ice Conversion}_{r_s}$  is change of  $\langle r_s \rangle$  due to the conversion of cloud ice to snow, that is, the recategorization of large ice crystals as snow crystals. We neglect the vertical transport of snow by large-scale ascent or descent of air because its values ( $O(1 \text{ cm s}^{-1})$ ) are much smaller than the speed of sedimentation or turbulent drafts ( $O(1 \text{ m s}^{-1})$ ).

[65] The snow budgets (2) for our three cloud cases are shown in Figures 9a, 10a, and 11a. The snow budgets are qualitatively similar in all three cloud cases and are somewhat simpler than the cloud water budgets. The generation and depletion of snow are dominated by just two processes, deposition/sublimation (crosses) and sedimentation (triangles). Therefore, these lines appear as approximate mirror images of each other in Figures 9–11. Snow grows by deposition in and below the liquid (mixed-phase) layer, and sublimates in the lower part of the virga layer. Sedimentation removes the snow aloft and places it in the virga layer below.

[66] Deposition and sublimation are proportional to the supersaturation with respect to ice. The rate of deposition is highest in the Oct 14 cloud. Figures 9b, 10b, and 11b display a profile of saturation ratio with respect to ice,

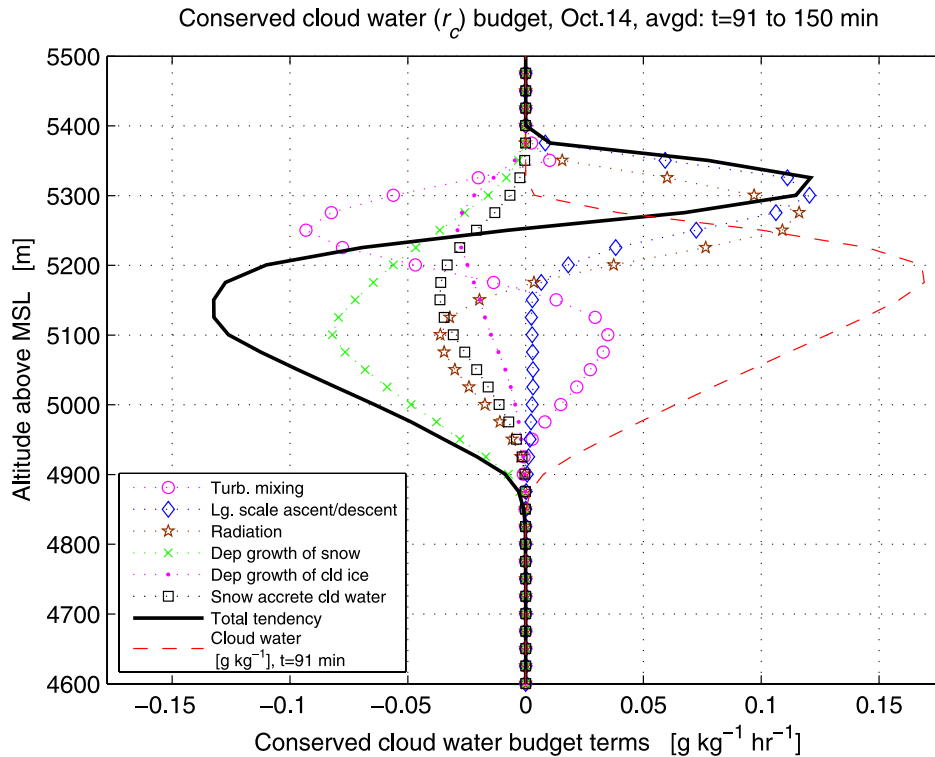


**Figure 7.** A budget of cloud water mixing ratio ( $r_c$ ) for the Oct 14 cloud case, time-averaged from  $t = 91$  to 150 min. Points in the negative region of the plot indicate that liquid is depleted by a process, while points in the positive region indicate that liquid is generated. The overall tendency of  $r_c$  is indicated by the solid line, and individual model processes are indicated by symbols. For reference, a dashed line indicates the cloud water mixing ratio profile at  $t = 91$  min. Large-scale ascent occurs, leading to development of new cloud and hence positive time tendency aloft.

$S_i = e/e_{s,i}$ , where  $e$  is vapor pressure and  $e_{s,i}$  is the equilibrium vapor pressure over ice. ( $S_i = 1$  implies exact saturation with respect to ice.) In a mixed-phase cloud that is saturated with respect to liquid,  $S_i$  is larger if the cloud is colder [see Rogers and Yau, 1989, Figure 9.3]. Among our cases, Oct 14 had the coldest cloud top temperature ( $-22^\circ\text{C}$ ), Nov 11 the next coldest ( $-16^\circ\text{C}$ ), and Nov 02 the warmest temperature ( $-13^\circ\text{C}$ ). Therefore, the Oct 14 case had the highest rate of deposition. Depositional rate is also affected by the thickness of the saturated layer, which allows snow growth over a thicker layer and hence a higher collective surface area of snow crystals below. Because the Nov 02 had a slightly thicker layer of high  $S_i$  than the Nov 11 case, the Nov 02 case had a slightly higher maximum deposition rate.

[67] Less influential processes are collection of cloud water by snow (squares in Figures 9–11) and conversion of cloud ice to snow (pluses in Figures 9–11), both of which must be always positive, and which tend to maximize in the middle to upper part of the liquid (mixed-phase) layer. Also small is turbulent mixing (transport) of snow (circles in Figures 9–11), which tends to be positive near cloud top and negative near the liquid cloud base. Because of the small turbulent transport, recycling of snow from the virga layer up into the liquid (mixed-phase) layer is small. In contrast, however, recycling of snow and vapor significantly extends cloud lifetime in the simulations of cirrus clouds by Köhler [1999].

#### 6.4. Liquid-Over-Snow Structure

[68] The budgets of  $r_c$  help shed light on the aforementioned question of why  $r_c$  maximizes near cloud top and  $r_s$  maximizes at lower altitudes (see Figure 5). If a thin layer of liquid forms at midlevels under typical temperature stratification, then there will be radiative cooling near cloud top and radiative warming near cloud base. This profile of heating is destabilizing and leads to small-scale turbulent convection. In our three (thin) clouds, the turbulence mixes the layer strongly enough to produce a quasi-adiabatic liquid profile with maximum  $r_c$  near cloud top. This is indicated by the fact that, for the  $r_c$  budget of the Oct 14 and Nov 02 cases, the turbulent mixing term is large at many altitudes (even though its vertical mean is small) (see Figures 6–8). In these two cases, turbulent mixing preserves quasi-adiabatic profiles by preventing radiation and large-scale ascent from generating too much liquid near cloud top, and preventing radiation and depositional growth of snow from depleting too much liquid near cloud base.

[69] Why does  $r_s$  maximize at altitudes below cloud top? For conceptual simplicity, ignore the vertical turbulent transport of snow, which is small (see Figures 9–11). As snow crystals start to grow, they become large enough to sediment downward, away from liquid cloud top. While the snow falls, it grows by deposition if the ambient air is supersaturated with respect to ice ( $S_i > 1$ ). In our three cloud cases,  $r_s$  maximizes near the altitude of zero supersaturation

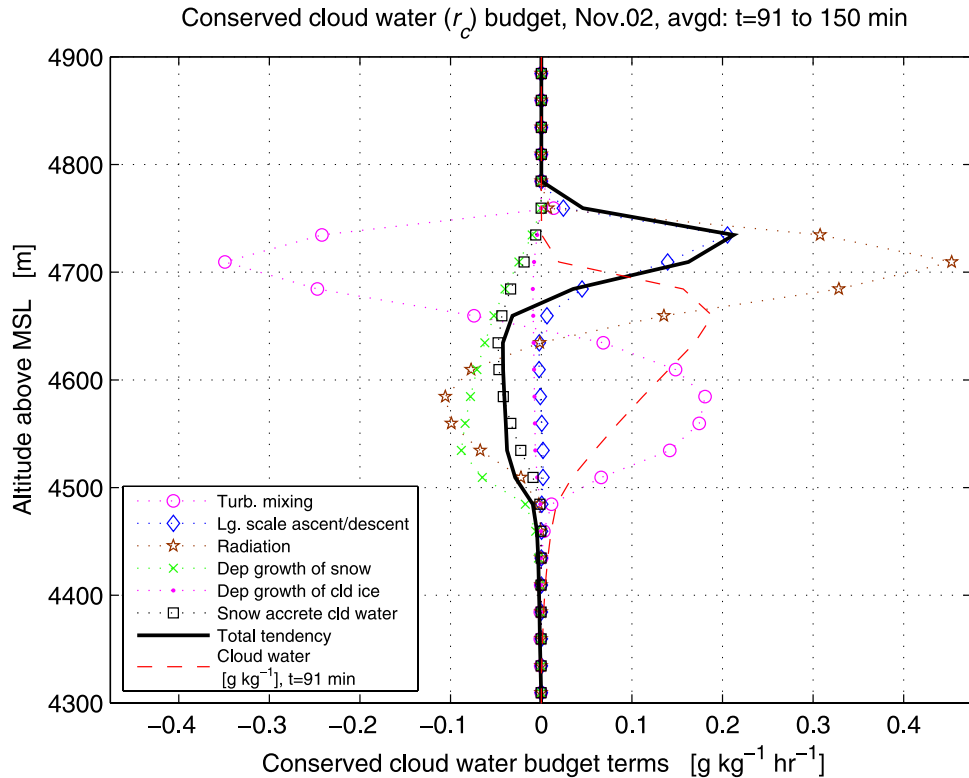


**Figure 8.** A budget of cloud water mixing ratio ( $r_c$ ) for the Nov 02 cloud case, time-averaged from  $t = 91$  to 150 min. Points in the negative region of the plot indicate that liquid is depleted by a process, while points in the positive region indicate that liquid is generated. The overall tendency of  $r_c$  is indicated by the solid line, and individual model processes are indicated by symbols. For reference, a dashed line indicates the cloud water mixing ratio profile at  $t = 91$  min. The profiles of the terms are qualitatively similar to those in the Oct 14 case, which also has positive large-scale ascent.

( $S_i = 1$ ), an altitude that resides below liquid cloud base. Snow at this altitude has had the opportunity to fall through a supersaturated layer of maximal thickness and grow along the way.

[70] This combination of liquid and snow effects in our three cloud simulations yields a maximum of liquid near cloud top and a maximum of snow at or below liquid cloud base, that is, a liquid-over-snow structure.

### 6.5. Deposition and Sublimation in the Snow Virga Layer

[71] We are particularly interested in examining the simulations of the virga layer, because the aircraft measurements of these cases were sparse, and therefore the simulations are our primary source of information. The flip side of this, of course, is that our simulated results have the caveat that some controlling factors in the lower part of the virga layer, such as saturation ratio, are measured only by rawinsonde. However, even if we cannot make firm conclusions about the historical details of what happened in these three particular cases, it is still instructive to explore modeled behavior given these realistic initial conditions.

[72] Our clouds exhibit a liquid-over-snow structure. The liquid boundaries of the mixed-phase layer in our simulations are demarcated by horizontal lines in Figures 9–11. The top of the virga layer coincides with the base of the

liquid (mixed-phase) layer, and the base of virga layer resides at the altitude where snow sublimates entirely. Near the base of the virga layer, snow sublimates, of course, but for each cloud case, the top of virga layer is a (nonliquid) region of depositional snow growth. The growth in the virga layer occurs because the top of the virga layer is supersaturated with respect to ice ( $S_i > 1$ , see Figures 9b, 10b, and 11b), and the sublimation occurs because the base of the virga is subsaturated ( $S_i < 1$ ). The subcloud growth region is to be expected because the liquid cloud base must be, of necessity, almost exactly saturated with respect to liquid, which implies that liquid cloud base is supersaturated with respect to ice. In our cases, the thickness of the supersaturated, snow-growth region below liquid cloud base is about 100 m in the Nov 02 case, 300 m in the Nov 11 case, and 1400 m in the Oct 14 case. The thickness of the growth region is tied somewhat to the liquid cloud base temperature. The reason is again that liquid cloud base is nearly saturated with respect to liquid, and hence the cloud base temperature determines the degree of supersaturation with respect to ice at the top of the virga layer. The greatest supersaturation occurs at a temperature of about  $-10^\circ$  to  $-16^\circ\text{C}$  [Rogers and Yau, 1989]. Therefore, hypothetically, if the temperature gradient below cloud and all other relevant factors were held fixed, clouds with cloud-base temperatures of about  $-10^\circ$  to  $-16^\circ\text{C}$  would be expected to

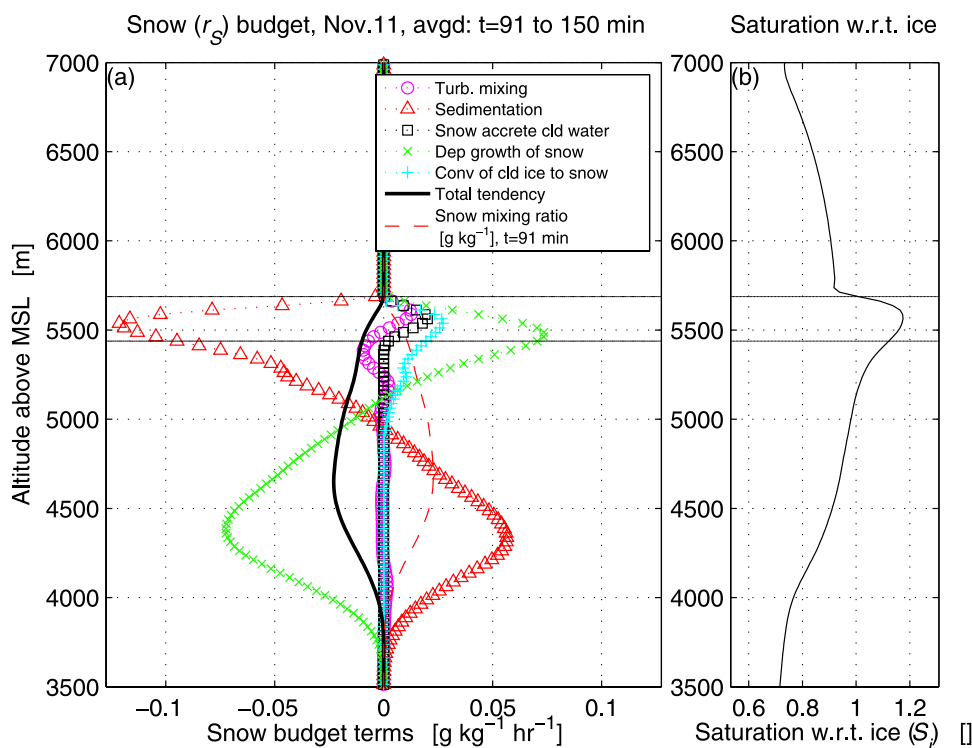


**Figure 9.** (a) A budget of snow mixing ratio  $r_S$  for the Nov 11 cloud case. The budget is integrated over a 1-h period from  $t = 91$  to 150 min. Points in the negative region of the plot indicate that snow is depleted by a process, while points in the positive region indicate that snow is generated. The overall tendency of snow mixing ratio is indicated by the solid line, and individual model processes are indicated by symbols. For reference, a dashed line indicates the snow mixing ratio profile at  $t = 91$  min, and horizontal lines indicate the liquid boundaries of the mixed-phase layer. The liquid boundaries are defined to be wherever cloud water mixing ratio (time-averaged from  $t = 91$  to 150 min) exceeds  $0.001 \text{ g kg}^{-1}$ . The simulation domain base (3000 m) is located below the bottom of the plot (3500 m). (b) A profile of the fraction of saturation with respect to ice, time-averaged from  $t = 91$  to 150 min. Horizontal lines indicate the boundaries of the liquid (mixed-phase) layer, which use the same definition as in Figure 9a. The deposition/sublimation and sedimentation terms dominate. Deposition occurs where  $S_i > 1$ , which includes a region immediately below liquid cloud base.

have a thicker region of snow growth below the liquid cloud base. Of course, the thickness also depends on the vapor and temperature profiles below cloud, and, in fact, in our cases the thickness appears to be influenced less by the liquid cloud base temperature than by the vapor profiles below cloud. For instance, the Oct 14 has a particularly extended region of supersaturation below liquid cloud base.

[73] Beneath the aforementioned snow growth region of the virga is a sublimation region, whose thickness is approximately 600 m in the Nov 02 case, 1400 m in the Nov 11 case, and 900 m in the Oct 14 case. The thickness of the sublimation region in our three cases appears to be strongly related to the degree of subsaturation. Where  $S_i \lesssim 0.8$ , the snow in our cases survives a fall of only several hundred more meters before vanishing. For instance, in the Oct 14 case, a value of  $r_S = 0.02 \text{ g kg}^{-1}$  extends over a large layer until  $r_S$  disappears over a few hundred meters where  $S_i < 0.8$  (Figure 10). One might have expected that the value of  $r_S$  at the zero-saturation level would have a larger effect, because, given a particular value of  $S_i$ , larger snow crystals can survive longer before vanishing. (In the

COAMPS single-moment microphysics scheme, crystal size increases as  $r_S$  increases.) However, one can show that if one assumes a balance between sublimation and sedimentation terms, then for the COAMPS microphysics, the depth over which snow vanishes via sublimation is proportional to  $(S_i - 1)^{-1}$ , but goes as a lower power of  $r_S$  ( $r_S^{1/2}$ ) [Larson and Smith, 2009]. Therefore, while the initial crystal size is important, it is not as important as the profile of  $S_i$ . Larson and Smith [2009] also study the sensitivity of these scalings to the exponents in the mass-diameter and fallspeed-diameter relationships for a variety of plate-like and dendritic habit types. The varying values of exponents leave the depth proportional to  $(S_i - 1)^{-1}$ , but the dependence on  $r_S$  varies from  $r_S^{0.4}$  to  $r_S^{0.77}$ .

[74] The deposition and sublimation of snow in the virga region leads to heating and cooling, respectively. Are these heating or cooling rates significant for our three cases? To address this question, we construct budgets of liquid water potential temperature,  $\theta_l$  (Figure 12). We find depositional heating rates and sublimative cooling rates of roughly 0.1 to 0.8  $\text{K h}^{-1}$ , which is comparable in magnitude to the

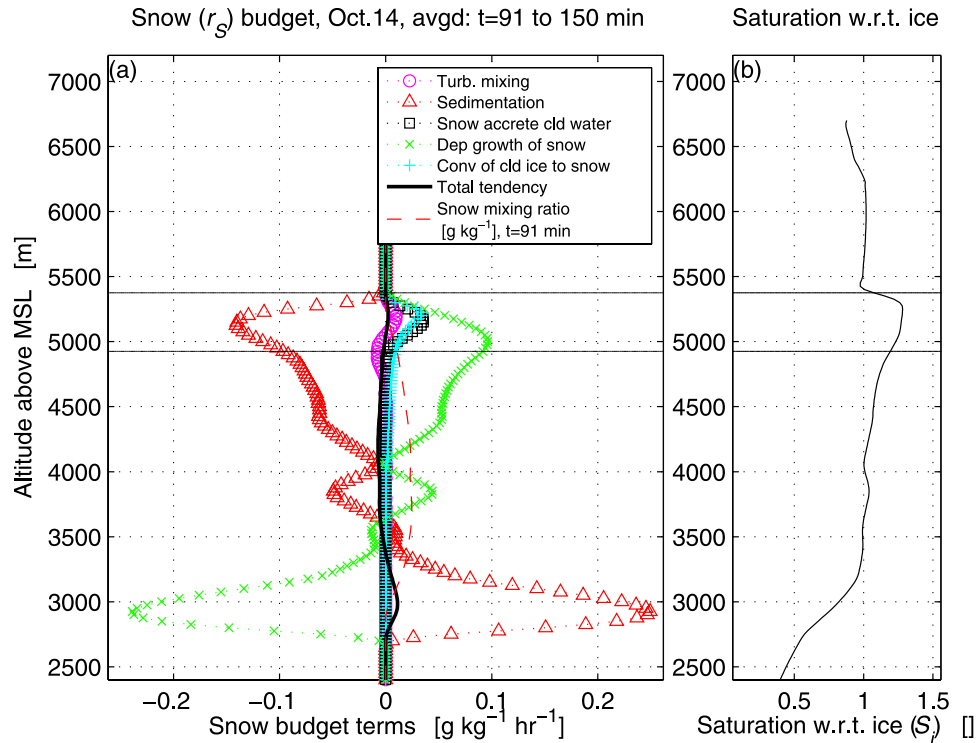


**Figure 10.** (a) A budget of snow mixing ratio  $r_s$  for the Oct 14 cloud case. The budget is integrated over a 1-h period from  $t = 91$  to 150 min. Points in the negative region of the plot indicate that snow is being depleted by a process, while points in the positive region indicate that snow is generated. The overall tendency of snow mixing ratio is indicated by the solid line, and individual model processes are indicated by symbols. For reference, a dashed line indicates the snow mixing ratio profile at  $t = 91$  min, and horizontal lines indicate the liquid boundaries of the mixed-phase layer. The liquid boundaries are defined to be wherever cloud water mixing ratio (time-averaged from  $t = 91$  to 150 min) exceeds  $0.001 \text{ g kg}^{-1}$ . The simulation domain base (2213 m) is located below the bottom of the plot. (b) A profile of the fraction of saturation with respect to ice, time-averaged from  $t = 91$  to 150 min. Horizontal lines indicate the liquid boundaries, which use the same definition as in Figure 10a. The budget is qualitatively similar to that for the Nov 11 case. The saturation ratio,  $S_i$ , exceeds 1 for a long distance below liquid cloud base, leading to a thick virga layer. Then  $S_i$  becomes small below 3000 m, leading to rapid sublimation there.

adiabatic heating or cooling due to large-scale descent or ascent, but smaller than the largest terms in the heat budget, such as within-cloud radiative transfer. Therefore, depositional heating and sublimative cooling are small, but not negligible.

## 7. Conclusions

[75] This paper has used large-eddy simulations of three altostratocumulus (ASc) clouds in order to explore the factors that influence cloud water and snow. The three (thin) ASc clouds possess a liquid-over-snow structure. Liquid peaks at cloud top because the liquid profiles are quasi-adiabatic, which in turn occurs because turbulence mixes the liquid cloud layer. Snow maximizes at or below liquid cloud base because snow can grow until it falls to the altitude at which the air is exactly saturated with respect to ice. This altitude resides below liquid cloud base. This is because in a mixed-phase cloud, the liquid cloud base tends to be nearly saturated with respect to liquid and therefore

supersaturated with respect to ice. Below the altitude of zero supersaturation, the air is subsaturated, and snow sublimates.

[76] We have constructed a budget of cloud water mixing ratio (see Figures 6–8), and it reveals several commonalities among the three clouds. Near cloud top, there is radiative cooling, which promotes condensation; near cloud base, there is radiative heating, which promotes evaporation. Depositional growth of snow removes liquid via the Bergeron-Findeisen process. Collection of droplets by snow also removes liquid, but is less effective than deposition. The largest difference among the three cases is that the Nov 11 cloud undergoes large-scale descent, which promotes evaporation of liquid, whereas the Oct 14 and Nov 02 clouds undergo large-scale ascent, which promotes condensation. The major processes relevant to generation and depletion of cloud water are summarized in a schematic diagram, Figure 13. The schematic lists all major processes. However, if we average vertically over the cloud system, then the most important terms in the cloud water budget

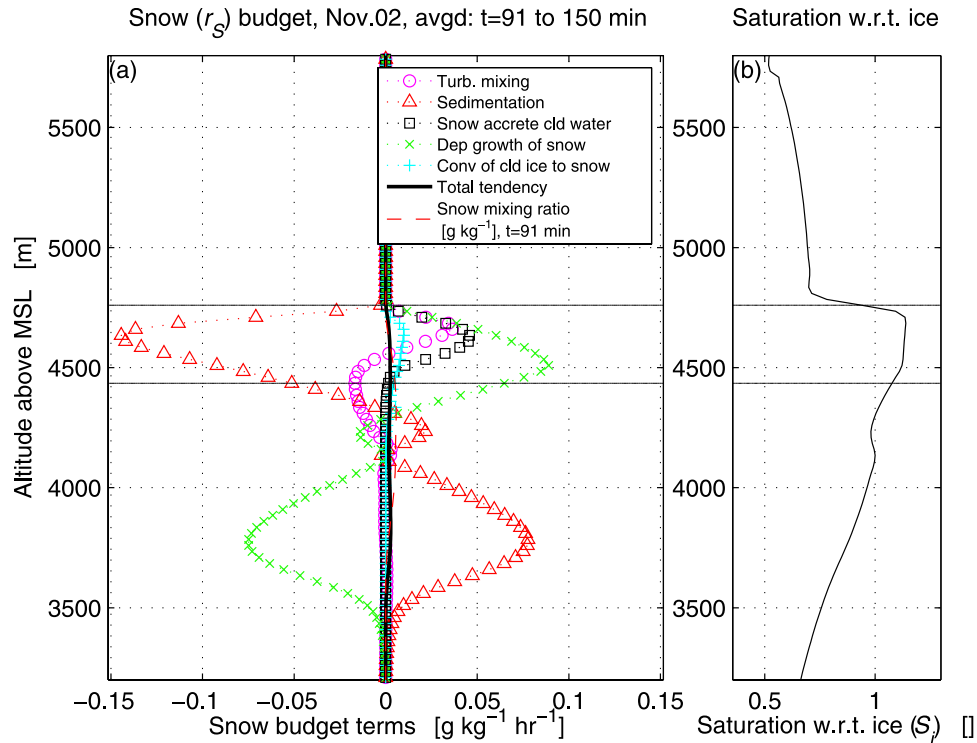


**Figure 11.** (a) A budget of snow mixing ratio  $r_s$  for the Nov 02 cloud case. The budget is integrated over a 1-h period from  $t = 91$  to 150 min. Points in the negative region of the plot indicate that snow is depleted by a process, while points in the positive region indicate that snow is generated. The overall tendency of snow mixing ratio is indicated by the solid line, and individual model processes are indicated by symbols. For reference, a dashed line indicates the snow mixing ratio profile at  $t = 91$  min, and horizontal lines indicate the liquid boundaries of the mixed-phase layer. The liquid boundaries are defined to be wherever cloud water mixing ratio (time-averaged from  $t = 91$  to 150 min) exceeds  $0.001 \text{ g kg}^{-1}$ . The simulation domain base (3097 m) is located below the bottom of the plot. (b) A profile of the fraction of saturation with respect to ice, time-averaged from  $t = 91$  to 150 min. Horizontal lines indicate the liquid boundaries, which use the same definition as in Figure 11a. The budget looks qualitatively similar to those for Nov 11 and Oct 14, with a balance between deposition/sublimation and sedimentation.

tend to be large-scale ascent/descent, depositional growth of snow, and radiative cooling/heating.

[77] We have also constructed a budget of snow mixing ratio (see Figures 9–11), which is simpler and turns out to be dominated by only two terms: deposition/sublimation, and sedimentation. Deposition begins near cloud top and extends below liquid cloud base. In the lower part of the virga region, there is sublimation. Sedimentation transports snow from the region of deposition above to the region of sublimation below. These snow processes are summarized schematically in Figure 14.

[78] The thickness of virga in our three cases appears to be related primarily to the vapor profile below liquid cloud base. Once the saturation ratio,  $S_i$ , drops below 0.8, snow disappears within several hundred meters. The virga thickness appears to be less sensitive to snow mixing ratio,  $r_s$ . This is plausible, given that it can be shown that the distance over which snow sublimates completely goes as the first power of  $(S_i - 1)$  but as only the square root of  $r_s$ .

[79] These simulations suggest several impediments to parameterization of AS<sub>c</sub> in large-scale models. First, AS<sub>c</sub> are thin. Although the cloud systems, including both liquid cloud and snow virga below, are 2 to 3 km thick, the liquid (mixed-phase) layers are only 0 to 700 m thick, and the regions of strong gradients near cloud top are only 100 to 200 m thick. Resolving such thin layers imposes significant computational cost [Marshall *et al.*, 2006]. Second, the vertical structure of all three clouds consists of a predominantly liquid (mixed-phase) layer over a snow virga layer below. Such a liquid-over-snow structure cannot be modeled by simple temperature-dependent microphysics schemes [Marshall *et al.*, 2006], which diagnose increasing liquid fraction as temperature increases. Third, for AS<sub>c</sub>, little is known about how best to parameterize entrainment at the base of the liquid cloud [Liu and Krueger, 1998]. In fact, in the Nov 11 and Oct 14 cases, *detrainment* occurs, in the sense that both cloud base and the turbulent layer base rise with time. Such detrainment has been studied little.

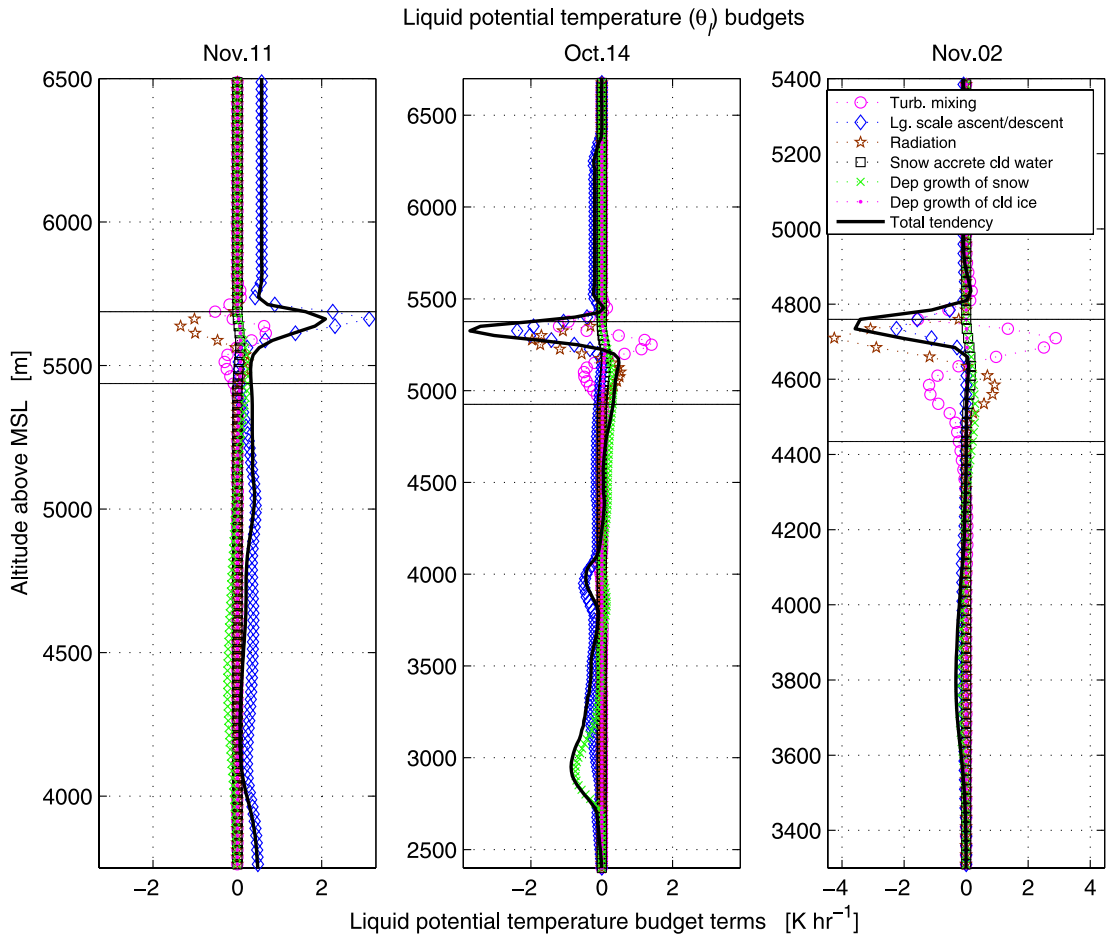


**Figure 12.** Budgets of liquid water potential temperature ( $\theta_l$ ) for (left) the Nov 11 cloud, (middle) the Oct 14 cloud, and (right) the Nov 02 cloud. The budgets are time-averaged from  $t = 91$  to 150 min. Thin solid horizontal lines denote the liquid boundaries of the mixed-phase cloud layer. Depositional/sublimative heating rates in the virga layer are small but not negligible.

### Processes affecting liquid water in a typical altostratocumulus cloud

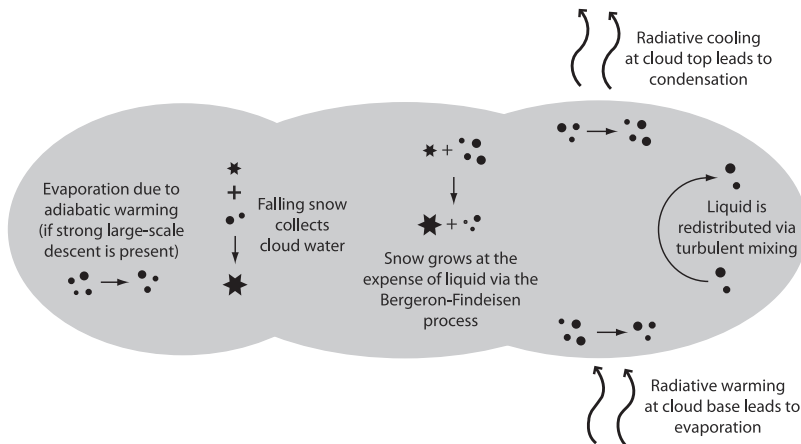


**Figure 13.** A schematic diagram showing the major processes that affect cloud water mixing ratio ( $r_c$ ) in an altostratocumulus cloud. These processes are included in the  $r_c$  budget (equation (1) and Figures 6–8).

### Processes affecting snow in a typical altostratocumulus cloud

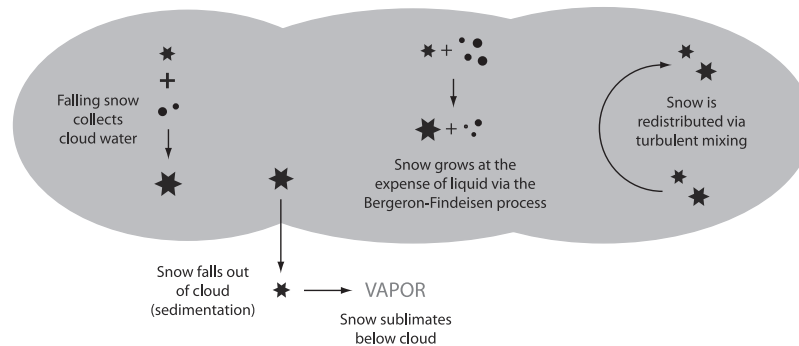


**Figure 14.** A diagram showing the major processes that affect snow mixing ratio ( $r_s$ ) in an altostratocumulus cloud. These processes correspond to the terms shown in the  $r_s$  budget (Figures 9–11).

[80] **Acknowledgments.** We thank three anonymous reviewers for their comments. A. J. Smith and V. E. Larson are grateful for financial support provided by grant ATM-0618818 from the National Science Foundation and by the UWM Research Growth Initiative. COAMPS<sup>®</sup> is a registered trademark of the Naval Research Laboratory.

### References

- Ackerman, A. S., et al. (2009), Large-eddy simulations of a drizzling, stratocumulus-topped marine boundary layer, *Mon. Weather Rev.*, *137*, 1083–1110, doi:10.1175/2008MWR2582.1.
- Boudala, F. S., G. A. Isaac, S. G. Cober, and Q. Fu (2004), Liquid fraction in stratiform mixed-phase clouds from in situ observations, *Q. J. R. Meteorol. Soc.*, *130*, 2919–2931, doi:10.1256/qj.03.153.
- Bower, K. N., S. J. Moss, D. W. Johnson, T. W. Choulaton, J. Latham, P. R. A. Brown, A. M. Blyth, and J. Cardwell (1996), A parametrization of the ice water content observed in frontal and convective clouds, *Q. J. R. Meteorol. Soc.*, *122*, 1815–1844.
- Brost, R. A., J. C. Wyngaard, and D. H. Lenschow (1982), Marine stratocumulus layers. Part II: Turbulence budgets, *J. Atmos. Sci.*, *39*, 818–836.
- Carey, L. D., J. Niu, P. Yang, J. A. Kankiewicz, V. E. Larson, and T. H. V. Haar (2008), The vertical profile of liquid and ice water content in mid-latitude mixed-phase altostratocumulus clouds, *J. Appl. Meteorol. Climatol.*, *47*, 2487–2495.
- Clark, P. D., T. W. Choulaton, P. R. A. Brown, P. R. Field, A. J. Illingworth, and R. J. Hogan (2005), Numerical modelling of mixed-phase frontal clouds observed during the CWVC project, *Q. J. R. Meteorol. Soc.*, *131*, 1677–1693.
- Cober, S. G., G. A. Isaac, A. V. Korolev, and J. W. Strapp (2001a), Assessing cloud phase conditions, *J. Appl. Meteorol.*, *40*, 1967–1983.
- Cober, S. G., G. A. Isaac, and J. W. Strapp (2001b), Characterizations of aircraft icing environments that include supercooled large drops, *J. Appl. Meteorol.*, *40*, 1984–2002.
- Colle, B. A., and Y. Zeng (2004), Bulk microphysical sensitivities within the MM5 for orographic precipitation. Part I: The Sierra 1986 event, *Mon. Weather Rev.*, *132*, 2780–2801.
- Colle, B. A., M. F. Garvert, J. B. Wolfe, C. F. Mass, and C. P. Woods (2005), The 13–14 December 2001 IMPROVE-2 event. Part III: Simulated microphysical budgets and sensitivity studies, *J. Atmos. Sci.*, *62*, 3535–3558.
- Cooper, W. A. (1986), Ice initiation in natural clouds, in *Precipitation Enhancement—A Scientific Challenge*, Meteorol. Monogr., vol. 43, pp. 29–32, Am. Meteorol. Soc., Boston, Mass.
- Curry, J. A. (1986), Interactions among turbulence, radiation, and microphysics in arctic stratus clouds, *J. Atmos. Sci.*, *43*, 90–106.
- Duynkerke, P. G., et al. (2004), Observations and numerical simulations of the diurnal cycle of the EUROCS stratocumulus case, *Q. J. R. Meteorol. Soc.*, *130*, 3269–3296.
- Falk, M. J., and V. E. Larson (2007), What causes partial cloudiness to form in multilayered midlevel clouds? A simulated case study, *J. Geophys. Res.*, *112*, D12206, doi:10.1029/2006JD007666.
- Ferrier, B. S. (1994), A double-moment multiple-phase four-class bulk ice scheme. Part I: Description, *J. Atmos. Sci.*, *51*, 249–280.
- Field, P. R. (1999), Aircraft observations of ice crystal evolution in an altostratus cloud, *J. Atmos. Sci.*, *56*, 1925–1941.
- Field, P. R., R. J. Hogan, P. R. A. Brown, A. J. Illingworth, T. W. Choulaton, P. H. Kaye, E. Hirst, and R. Greenaway (2004), Simultaneous radar and aircraft observations of mixed-phase cloud at the 100 m scale, *Q. J. R. Meteorol. Soc.*, *130*, 1877–1904.
- Fleishauer, R. P., V. E. Larson, and T. H. Vonder Haar (2002), Observed microphysical structure of midlevel, mixed-phase clouds, *J. Atmos. Sci.*, *59*, 1779–1804.
- Fletcher, N. H. (1962), *The Physics of Rainclouds*, 386 pp., Cambridge Univ. Press, Cambridge, U. K.
- Fridlind, A. M., A. S. Ackerman, G. McFarquhar, G. Zhang, M. R. Poellot, P. J. DeMott, A. J. Prenni, and A. J. Heymsfield (2007), Ice properties of single-layer stratocumulus during the Mixed-Phase Arctic Cloud Experiment: 2. Model results, *J. Geophys. Res.*, *112*, D24202, doi:10.1029/2007JD008646.
- Garrett, T. J., and C. Zhao (2006), Increased Arctic cloud longwave emissivity associated with pollution from mid-latitudes, *Nature*, *440*, 787–789, doi:10.1038/nature04636.
- Gedzelman, S. D. (1988), In praise of altocumulus, *Weatherwise*, *41*(2), 143–149.
- Golaz, J.-C., S. Wang, J. D. Doyle, and J. M. Schmidt (2005), Second and third moment vertical velocity budgets derived from COAMPS-LES, *Boundary Layer Meteorol.*, *116*, 487–517.
- Harrington, J. Y., and P. Q. Olsson (2001), A method for the parameterization of cloud optical properties in bulk and bin microphysical models: Implications for arctic cloudy boundary layers, *Atmos. Res.*, *57*, 51–80.
- Harrington, J. Y., T. Reisin, W. R. Cotton, and S. M. Kreidenweis (1999), Cloud resolving simulations of Arctic stratus. Part II: Transition-season clouds, *Atmos. Res.*, *51*, 45–75.
- Haulman, D. L. (2003), U.S. unmanned aerial vehicles in combat, 1991–2003, report, 18 pp., Air Force Hist. Res. Agency, Maxwell AFB, Ala.
- Heymsfield, A. J., L. M. Milosevich, A. Slingo, K. Sassen, and D. O. Starr (1991), An observational and theoretical study of highly supercooled altocumulus, *J. Atmos. Sci.*, *48*, 923–945.
- Hobbs, P. V., and A. L. Rangno (1985), Ice particle concentrations in clouds, *J. Atmos. Sci.*, *42*, 2523–2549.
- Hobbs, P. V., and A. L. Rangno (1998), Microstructures of low and middle-level clouds over the Beaufort Sea, *Q. J. R. Meteorol. Soc.*, *124*, 2035–2071.
- Hobbs, P. V., A. L. Rangno, M. Shupe, and T. Uttal (2001), Airborne studies of cloud structures over the Arctic Ocean and comparisons with retrievals from ship-based remote sensing measurements, *J. Geophys. Res.*, *106*, 15,029–15,044.
- Hodur, R. M. (1997), The Naval Research Laboratory’s Coupled Ocean/Atmosphere Mesoscale Prediction System (COAMPS), *Mon. Weather Rev.*, *125*, 1414–1430.
- Illingworth, A. J., et al. (2007), CLOUDNET: Continuous evaluation of cloud profiles in seven operational models using ground-based observations, *Bull. Am. Meteorol. Soc.*, *88*, 883–898.
- Jiang, H., W. R. Cotton, J. O. Pinto, J. A. Curry, and M. J. Weissbluth (2000), Cloud resolving simulations of mixed-phase Arctic stratus observed during BASE: Sensitivity to concentration of ice crystals and large-scale heat and moisture advection, *J. Atmos. Sci.*, *57*, 2105–2112.

- Kattsov, V. M., and E. Källén (2005), Future climate change: Modeling and scenarios for the Arctic, in *Arctic Climate Impact Assessment—Scientific Report*, pp. 99–150, Cambridge Univ. Press, Cambridge, U. K.
- Katzfey, J. J., and B. F. Ryan (2000), Midlatitude frontal clouds: GCM-scale modeling implications, *J. Clim.*, *13*, 2729–2745.
- Khairoutdinov, M., and D. A. Randall (2003), Cloud resolving modeling of the ARM Summer 1997 IOP: Model formulation, results, uncertainties, and sensitivities, *J. Atmos. Sci.*, *60*, 607–624.
- Klein, S. A., et al. (2009), Intercomparison of model simulations of mixed-phase clouds observed during the ARM Mixed-Phase Arctic Cloud Experiment. Part I: Single-layer cloud, *Q. J. R. Meteorol. Soc.*, doi:10.1002/qj.416, in press.
- Köhler, M. (1999), Explicit prediction of ice clouds in general circulation models, Ph.D. thesis, 167 pp., Univ. of Calif., Los Angeles, Los Angeles.
- Korolev, A. V., G. A. Isaac, S. G. Cober, J. W. Strapp, and J. Hallett (2003), Microphysical characterization of mixed-phase clouds, *Q. J. R. Meteorol. Soc.*, *129*, 39–65.
- Korolev, A. V., G. A. Isaac, J. W. Strapp, S. G. Cober, and H. W. Barker (2007), In situ measurements of liquid water content profiles in midlatitude stratiform clouds, *Q. J. R. Meteorol. Soc.*, *133*, 1693–1699.
- Larson, V. E., and A. J. Smith (2009), An analytic scaling law for glaciation rate in thin mixed-phase layer clouds, *J. Atmos. Sci.*, in press.
- Larson, V. E., R. P. Fleishauer, J. A. Kankiewicz, D. L. Reinke, and T. H. Vonder Haar (2001), The death of an altocumulus cloud, *Geophys. Res. Lett.*, *28*, 2609–2612.
- Larson, V. E., A. J. Smith, M. J. Falk, K. E. Kotenberg, and J.-C. Golaz (2006), What determines altocumulus dissipation time?, *J. Geophys. Res.*, *111*, D19207, doi:10.1029/2005JD007002.
- Larson, V. E., K. E. Kotenberg, and N. B. Wood (2007), An analytic long-wave radiation formula for liquid layer clouds, *Mon. Weather Rev.*, *135*, 689–699.
- Lawson, R. P., B. A. Baker, C. G. Schmitt, and T. L. Jensen (2001), An overview of microphysical properties of Arctic clouds observed in May and July 1998 during FIRE ACE, *J. Geophys. Res.*, *106*, 14,989–15,014.
- Lazarus, S. M., S. K. Krueger, and G. G. Mace (2000), A cloud climatology of the Southern Great Plains ARM CART, *J. Clim.*, *13*, 1762–1775.
- Lebo, Z. J., N. C. Johnson, and J. Y. Harrington (2008), Radiative influences on ice crystal and droplet growth within mixed-phase stratus clouds, *J. Geophys. Res.*, *113*, D09203, doi:10.1029/2007JD009262.
- Liu, S., and S. K. Krueger (1998), Numerical simulations of altocumulus using a cloud resolving model and a mixed layer model, *Atmos. Res.*, *47–48*, 461–474.
- Long, M. L. (2003), COAMPS™ version 3 model description—General theory and equations, *NRL Publ. NRL/PU/7500–03-448*, Tech. Inf. Serv. Branch, Nav. Res. Lab., Washington, D. C.
- Lynn, B. H., A. P. Khain, J. Dudhia, D. Rosenfeld, A. Pokrovsky, and A. Seifert (2005), Spectral (bin) microphysics coupled with a mesoscale model (MM5). Part I: Model description and first results, *Mon. Weather Rev.*, *133*, 44–58.
- Marquis, J., and J. Y. Harrington (2005), Radiative influences on drop and cloud condensation nuclei equilibrium in stratocumulus, *J. Geophys. Res.*, *110*, D10205, doi:10.1029/2004JD005401.
- Marshall, J. H., S. Dobbie, and R. J. Hogan (2006), Evaluation of a large-eddy model simulation of a mixed-phase altocumulus cloud using microwave radiometer, lidar, and Doppler radar data, *Q. J. R. Meteorol. Soc.*, *132*, 1693–1715.
- McFarquhar, G. M., G. Zhang, M. R. Poellot, G. L. Kok, R. McCoy, T. Tooman, A. Fridlind, and A. J. Heymsfield (2007), Ice properties of single-layer stratocumulus during the Mixed-Phase Arctic Cloud Experiment: 2. Observations, *J. Geophys. Res.*, *112*, D24201, doi:10.1029/2007JD008633.
- Meyers, M. P., P. J. D. Mott, and W. R. Cotton (1992), New primary ice-nucleation parameterizations in an explicit cloud model, *J. Appl. Meteorol.*, *31*, 708–721.
- Misra, V., M. K. Yau, and N. Badrinath (2000), Atmospheric water species budget in mesoscale simulations of lee cyclones over the Mackenzie River Basin, *Tellus, Ser. A*, *52*(2), 140–161.
- Morrison, H., J. A. Curry, and V. I. Khvorostyanov (2005), A new double-moment microphysics parameterization for application in cloud and climate models. Part I: Description, *J. Atmos. Sci.*, *62*, 1665–1677.
- Morrison, H., J. O. Pinto, J. A. Curry, and G. M. McFarquhar (2008), Sensitivity of modeled arctic mixed-phase stratocumulus to cloud condensation and ice nuclei over regionally varying surface conditions, *J. Geophys. Res.*, *113*, D05203, doi:10.1029/2007JD008729.
- Niu, J., L. D. Carey, P. Yang, and T. H. Vonder Haar (2008), Optical properties of a vertically inhomogeneous mid-latitude mid-level mixed-phase altocumulus in the infrared region, *Atmos. Res.*, *88*, 234–242.
- Olsson, P. Q., and J. Y. Harrington (2000), Dynamics and energetics of the cloudy boundary layer in simulations of off-ice flow in the marginal ice zone, *J. Geophys. Res.*, *105*, 11,889–11,899.
- Pinto, J. O. (1998), Autumnal mixed-phase cloudy boundary layers in the Arctic, *J. Atmos. Sci.*, *55*, 2016–2017.
- Pinto, J. O., J. A. Curry, and J. M. Intrieri (2001), Cloud-aerosol interactions during autumn over Beaufort Sea, *J. Geophys. Res.*, *106*, 15,077–15,097.
- Prenni, A. J., J. Y. Harrington, M. Tjernström, P. J. DeMott, A. Avramov, C. N. Long, S. M. Kreidenweis, P. Q. Olsson, and J. Verlinde (2007), Can ice-nucleating aerosols affect Arctic seasonal climate?, *Bull. Am. Meteorol. Soc.*, *88*, 541–550.
- Rauber, R. M., and A. Tokay (1991), An explanation for the existence of supercooled water at the top of cold clouds, *J. Atmos. Sci.*, *55*, 2016–2038.
- Reisin, T., Z. Levin, and S. Tzivion (1996), Rain production in convective clouds as simulated in an axisymmetric model with detailed microphysics. Part I: Description of the model, *J. Atmos. Sci.*, *53*, 497–519.
- Rinke, A., et al. (2006), Evaluation of an ensemble of Arctic regional climate models: spatiotemporal fields during the SHEBA year, *Clim. Dyn.*, *26*, doi:10.1007/s00382-005-0095-3.
- Rogers, R. R., and M. K. Yau (1989), *A Short Course in Cloud Physics*, 3rd ed., 290 pp., Elsevier, New York.
- Rutledge, S. A., and P. V. Hobbs (1983), The mesoscale and microscale structure of organization of clouds and precipitation in midlatitude cyclones. VIII: A model for the “seeder-feeder” process in warm-frontal rainbands, *J. Atmos. Sci.*, *40*, 1185–1206.
- Ryan, B. F., et al. (2000), Simulations of a cold front by cloud-resolving, limited-area, and large-scale models, and a model evaluation using in situ and satellite observations, *Mon. Weather Rev.*, *128*, 3218–3235.
- Sassen, K., and V. I. Khvorostyanov (2007), Microphysical and radiative properties of mixed-phase altocumulus: A model evaluation of glaciation effects, *Atmos. Res.*, *84*, 390–398.
- Schubert, W. H., J. S. Wakefield, E. J. Steiner, and S. K. Cox (1979), Marine stratocumulus convection. Part I: Governing equations and horizontally homogeneous solutions, *J. Atmos. Sci.*, *36*, 1286–1307.
- Shettle, E. P., and J. A. Weinman (1970), The transfer of solar irradiance through inhomogeneous turbid atmospheres evaluated by Eddington’s approximation, *J. Atmos. Sci.*, *27*, 1048–1055.
- Smith, R. N. B. (1990), A scheme for predicting layer clouds and their water content in a general circulation model, *Q. J. R. Meteorol. Soc.*, *116*, 435–460.
- Starr, D. O., and S. K. Cox (1985), Cirrus clouds. Part II: Numerical experiments on the formation and maintenance of cirrus, *J. Atmos. Sci.*, *42*, 2682–2694.
- Stevens, B., et al. (2003), Dynamics and chemistry of marine stratocumulus—DYCOMS-II, *Bull. Am. Meteorol. Soc.*, *84*, 579–593.
- Sun, Z., and K. P. Shine (1994), Studies of the radiative properties of ice and mixed-phase clouds, *Q. J. R. Meteorol. Soc.*, *120*, 111–137.
- Verlinde, J., et al. (2007), The mixed-phase Arctic cloud experiment, *Bull. Am. Meteorol. Soc.*, *88*, 205–221.
- Walsh, J. E., V. M. Kattsov, W. L. Chapman, V. Govorkova, and T. Pavlova (2002), Comparison of Arctic climate simulations by uncoupled and coupled global models, *J. Clim.*, *15*, 1429–1446.
- Wang, Z., K. Sassen, D. N. Whiteman, and B. B. Demoz (2004), Studying altocumulus with ice virga using ground-based active and passive remote sensors, *J. Appl. Meteorol.*, *43*, 449–460.
- Weaver, C. P., J. R. Norris, N. D. Gordon, and S. A. Klein (2005), Dynamical controls on sub-global climate model grid-scale cloud variability for Atmospheric Radiation Measurement Program (ARM) case 4, *J. Geophys. Res.*, *110*, D15S05, doi:10.1029/2004JD005022.
- Xu, K.-M., et al. (2005), Modeling springtime shallow frontal clouds with cloud-resolving and single-column models, *J. Geophys. Res.*, *110*, D15S04, doi:10.1029/2004JD005153.
- Zhang, M. H., et al. (2005), Comparing clouds and their seasonal variations in 10 atmospheric general circulation models with satellite measurements, *J. Geophys. Res.*, *110*, D15S02, doi:10.1029/2004JD005021.

L. D. Carey, Earth System Sciences Center, National Space Science and Technology Center, University of Alabama in Huntsville, 320 Sparkman Drive, Huntsville, AL 35899, USA.

J. A. Kankiewicz, WindLogics, Inc., St. Paul, MN 55108, USA.

V. E. Larson, Department of Mathematical Sciences, University of Wisconsin-Milwaukee, Milwaukee, WI 53201, USA. (vlarson@uwm.edu)

J. Niu, IMG, Center for Satellite Applications and Research, NESDIS, NOAA, Camp Springs, MD 20746, USA.

A. J. Smith, School of Meteorology, University of Oklahoma, 120 David L. Boren Boulevard, Norman, OK 73072-7307, USA. (adam.j.smith-1@ou.edu)